

AD A 048797

18 19
AFRPL TR-77-44

2
NW

6
**Monopropellant Thruster Exhaust Plume
Contamination Measurements**

9 Final Report. Jun 74 - Jun 75

JET PROPULSION LABORATORY
4800 OAK GROVE DRIVE
PASADENA, CALIFORNIA 91103

12
AUTHORS: B. K. BAERWALD
R. S. PASSAMANECK

11 SEP 1977

12 65

JPL-141-77-61

39301 471
Approved for Public Release;
Distribution Unlimited

AD No. _____
ODC FILE COPY

AIR FORCE ROCKET PROPULSION LABORATORY
DIRECTOR OF SCIENCE AND TECHNOLOGY
AIR FORCE SYSTEMS COMMAND
EDWARDS AFB, CALIFORNIA 93523

191 150


NOTICES

When U.S. Government drawings, specifications, or other data are used for any purpose other than a definitely related government procurement operation, the Government thereby incurs no responsibility nor any obligation whatsoever, and the fact that the Government may have formulated, furnished, or in any way supplied the said drawings, specifications or other data, is not to be regarded by implication or otherwise, or in any manner licensing the holder or any other person or corporation, or conveying any rights or permission to manufacture, use, or sell any patented invention that may in any way be related thereto.

FOREWORD


This report was submitted by the Jet Propulsion Laboratory, 4800 Oak Grove Drive, Pasadena, California 91103 under P.O. No. 5730-75-6, JON 573009AW with the Air Force Rocket Propulsion Laboratory, Edwards AFB, CA 93523.

This report has been reviewed by the Information Office/DOZ and is releaseable to the National Technical Information Service (NTIS). At NTIS it will be available to the general public, including foreign nations. This technical report has been reviewed and is approved for publication; it is unclassified and suitable for general public release.


ERIC G. LUND, Lt., USAF
Project Manager


J. DANIEL STEWART
Chief, Plume Technology Section

FOR THE COMMANDER


WILLIAM MORRIS, Colonel, USAF
Chief, Technology Division

UNCLASSIFIED

SECURITY CLASSIFICATION OF THIS PAGE (When Data Entered)

REPORT DOCUMENTATION PAGE		READ INSTRUCTIONS BEFORE COMPLETING FORM
1. REPORT NUMBER AFRPL TR-77-44	2. GOVT ACCESSION NO.	3. RECIPIENT'S CATALOG NUMBER
4. TITLE (and Subtitle) MONOPROPELLANT THRUSTER EXHAUST PLUME CONTAMINATION MEASUREMENTS		5. TYPE OF REPORT & PERIOD COVERED June 1974 - June 1976
		6. PERFORMING ORG. REPORT NUMBER JPL Publication 77-61
7. AUTHOR(s) R. K. Baerwald, R. S. Passamaneck		8. CONTRACT OR GRANT NUMBER(s) PRO 5730-75-6
9. PERFORMING ORGANIZATION NAME AND ADDRESS Jet Propulsion Laboratory 4800 Oak Grove Drive Pasadena, California 91103		10. PROGRAM ELEMENT, PROJECT, TASK AREA & WORK UNIT NUMBERS JON 573009AW
11. CONTROLLING OFFICE NAME AND ADDRESS Air Force Rocket Propulsion Laboratory/DY Edwards AFB, California 93523		12. REPORT DATE September 1977
		13. NUMBER OF PAGES 63
14. MONITORING AGENCY NAME & ADDRESS (if different from Controlling Office)		15. SECURITY CLASS. (of this report) UNCLASSIFIED
		15a. DECLASSIFICATION/DOWNGRADING SCHEDULE
16. DISTRIBUTION STATEMENT (of this Report) APPROVED FOR PUBLIC RELEASE; DISTRIBUTION UNLIMITED		
17. DISTRIBUTION STATEMENT (of the abstract entered in Block 20, if different from Report)		
18. SUPPLEMENTARY NOTES		
19. KEY WORDS (Continue on reverse side if necessary and identify by block number) Monopropellant Contamination Thruster Crystal deposition Plume QCMs		
20. ABSTRACT (Continue on reverse side if necessary and identify by block number) The potential spacecraft contaminants in the exhaust plume of a 0.89N (0.2 lbf) monopropellant hydrazine thruster were measured in an ultrahigh vacuum molecular sink facility. The engine plume was directed toward five quartz crystal micro-balances (QCMs) located at angles of approximately 0°, ± 15°, and ± 30° with respect to the nozzle centerline. The crystal temperatures were controlled such that the mass adhering to the crystal surface at temperatures of from 106°K to 256°K could be measured. Thruster duty cycles of 25 ms on/5 seconds off,		

D D C
JAN 25 1978
F

UNCLASSIFIED

SECURITY CLASSIFICATION OF THIS PAGE (When Data Entered)

100 ms on/ 10 seconds off, and 200 ms on/20 seconds off were investigated. The change in contaminant production with thruster life was assessed by subjecting the thruster to a 100,000 pulse aging sequence and comparing the before and after contaminant deposition rates.

Approximately 25% of the plume centerline mass flux was found to adhere to the QCM crystal surface at 106°K, around 1% at 144°K, and less than 0.05% at 172°K and 200°K. Contaminant mass deposition at higher temperatures was too low for quantitative determination.

The predominant contaminant at a surface temperature of 106°K was postulated to be ammonia, while water and undecomposed hydrazine probably represent the primary constituents remaining on a surface at 144°K. The deposits on higher temperature surfaces were much more difficult to characterize, but small amounts of water and hydrazine, which subsequently revaporize, hydrazine compounds, and aniline or aniline-derived hydrocarbons are likely candidates.


Duty cycle appeared to have little effect on contaminant production except as the duty cycle influenced the average propellant flowrate.

A decrease in the contaminants measured by the 144°K surface and an increase in deposits on the 172°K and 200°K surfaces were noted as the thruster was aged.

It was found that the shape of the plume within 30° of the nozzle centerline could be adequately described by the analytical approximation of Hill and Draper if the necessary calculations were performed using a ratio of specific heats of 1.4 for the exhaust gases.

TABLE OF CONTENTS

I.	INTRODUCTION	7
II.	EXPERIMENTAL FACILITY	9
	A. Molecular Sink Vacuum Chamber	9
	B. Microbalance Instrumentation	13
	C. Propulsion System	17
	D. Data Acquisition System	25
	E. Facility Operation	25
III.	TEST DESCRIPTION	27
IV.	RESULTS	29
	A. Plume Shape and Data Interpretation	32
	B. Contaminant Capture as a Function of Surface Temperature . .	34
	C. Duty Cycle Effects	39
	D. Thruster Life Effects	42
	E. Effect of Pulse Train Transients	49
V.	CONCLUSIONS AND RECOMMENDATIONS	49
	REFERENCES	52
	APPENDIXES	
	A. Derivation of Relations Pertaining to the Quartz Crystal Microbalance	55
	B. Data Reduction	58
	DEFINITION OF SYMBOLS	62

ACCESSION for	
NTIS	Write Section <input checked="" type="checkbox"/>
RDC	Buff Section <input type="checkbox"/>
UNANNOUNCED	<input type="checkbox"/>
U.S. EDUCATION	
BY	
DISTRIBUTION/AVAILABILITY CODES	
SPECIAL	
	

LIST OF ILLUSTRATIONS

1. MOLSINK Vacuum Chamber and Auxiliary Equipment	10
2. Molecular Sink (MOLSINK) Ultrahigh-Vacuum Chamber	11
3. General Arrangement of Systems in the MOLSINK Facility	12
4. Quartz Crystal Electrodes and Demonstration of the Thickness Vibration Mode	15
5. Doublet QCM	15
6. Quartz Crystal Doublet	16
7. Schematic Diagram of a Variable Temperature QCM Unit	18
8. A View of a QCM Unit With the Teflon Collimator Removed	19
9. QCMs as Viewed From the Thruster	20
10. QCM Orientation and Thruster Position in MOLSINK Chamber	22
11. Hamilton Standard REA 10-18 Thruster as Installed in MOLSINK Facility	23
12. Thermal Control System for Propellant Lines	24
13. Hydrazine Propellant Module Flow System Schematic Diagram	26
14. Measurement Repeatability Relative to Center Crystal	33
15. Effect of QCM Crystal Temperature on Centerline Mass Deposition Rate	35
16. Effect of Water Addition to Propellant	38
17. Effects of Duty Cycle	40
18. Centerline Deposition Versus Propellant Flowrate	41
19. Effects of Pulse Width	43
20. Effects of Thruster Life at a Crystal Temperature of 144°K	44
21. Effects of Thruster Life at Crystal Temperatures of 172°K and 200°K	45

22.	Effects of Thruster Life	46
23.	Thruster Chamber Pressure Pulse Shape During Aging Sequence (90 ms Pulse Width)	48
24.	Effects of Pulse Train Transients	50
B-1.	Beat Frequency Versus Time for QCM "I" During Run 2	59
B-2.	Mass Deposition Rate as Derived From Figure B-1	60

LIST OF TABLES

I.	Nominal Characteristics of Hamilton Standard REA 10-18 Thruster	17
II.	Nominal Temperatures of Thermally Controlled Components	21
III.	Test Sequence	28
IV.	Thruster Aging Sequence	30
V.	Summary of Results	31
VI.	Gas Sample Constituents and Capture Temperature	37

1. INTRODUCTION

Monopropellant hydrazine thruster technology has advanced to a state where almost all unmanned spacecraft utilize this type of propulsion for attitude control, orbit maneuvers, and trajectory correction. In addition to the simplicity and reliability offered by these monopropellant hydrazine systems, the potential spacecraft contaminants generated by the catalytic decomposition of hydrazine are relatively innocuous compared with the products of bipropellant rocket engines. Testing in space simulation facilities has demonstrated negligible effects upon solar cells, thermal control coatings, and radiant coolers, even when subjected to direct impingement by monopropellant rocket plumes (Refs. 1-3). Analysis has further indicated that such contamination of sensitive spacecraft surfaces is probably not a problem if the surface can be maintained above 215°K (Ref. 4). Flight measurements utilizing a 200°K quartz crystal microbalance (QCM) located in the backflow region of a hydrazine thruster plume could not distinguish the effects of thruster operation (Ref. 5). However, despite the seemingly favorable contamination picture presented by hydrazine systems, there are still contamination concerns peculiar to this type of propulsion.

Catalyst loss is one of the primary factors limiting the life of hydrazine thrusters (Ref. 6). The breakup of catalyst particles is generally attributed to thermal stresses or large pressure gradients within a catalyst pellet (Ref. 7); the resulting fines are expelled through the rocket nozzle at high velocities. This catalyst attrition phenomenon is especially severe on startup when the reactor bed is at or below earth ambient temperatures; losses of 30% or more of the catalyst mass have been reported (Ref. 8) after repeated cold starts. Much effort has been expended in defining the engine design practices and duty cycle effects on catalyst attrition (Refs. 9-11), and treatment or sorting of the catalyst particles themselves also shows promise of reducing catalyst loss (Ref. 12). Test results with an unspecified catalyst type indicate that the fines produced will be of less than 20 μm and will be primarily confined to a region of the exhaust plume located within 12° of the nozzle centerline (Ref. 2). Assuming good design practices on the part of the engine manufacturer and careful thruster placement by the spacecraft designer, contamination or mechanical damage to the spacecraft due to catalyst particle ejection will probably not be of serious concern.

Perhaps the most serious contamination problem presented by hydrazine thruster operation is in the area of exhaust product deposition on scientific instrument surfaces which are maintained at temperatures well below the 200°K limit previously discussed. The optical surfaces of infrared sensors, for example, are particularly susceptible to performance degradation through increased absorption and scattering of incident radiation by cryodeposits. Since the highly polished mirrors of these instruments may be maintained below 20°K (Ref. 13) to reduce the effects of internally generated noise, the cryotrapping of any incident rocket exhaust plume gases is almost a certainty. As the gases from a monopropellant rocket engine will not, in most cases, be trapped by the higher temperature surfaces of the spacecraft, the sensor may receive reflected contaminants from any surface within its field of view. It thus becomes necessary to define both the rocket exhaust plume flow field and the expected quantity and species of any suspected contaminants.

The primary exhaust constituents from the decomposition of hydrazine are nitrogen, hydrogen, and ammonia. The relative concentration of these products depends upon the amount of ammonia which dissociates into hydrogen and nitrogen, an endothermic reaction which is controlled primarily by catalyst bed design. The hydrogen will probably never constitute a hazard to sensitive spacecraft surfaces; the nitrogen will condense only on the lowest temperature optics ($< 26^{\circ}\text{K}$) and at that will probably present minimal optical disturbances (Ref. 14) compared to the other contaminants. Ammonia will probably begin to accumulate on surfaces at around 70°K (Ref. 15) in a space environment.

In addition to these products, undecomposed hydrazine may be expelled from the engine. Random amounts of gaseous hydrazine have been detected at various pulsing duty cycles and during steady state operation, even after the thruster has achieved thermal equilibrium (Refs. 16-19). The ejection of undecomposed hydrazine is particularly likely during a vacuum cold start with low temperature propellant, which may in fact cause liquid to be expelled from the engine. The discharge of undecomposed hydrazine will become much worse if the thruster is exhibiting the performance loss commonly referred to as "washout." This phenomena may occur during either steady state or pulse mode operation; decomposition in the catalytic reactor becomes erratic and may cease altogether, allowing unreacted propellant to leave the nozzle (Ref. 20). Frozen hydrazine has been reported hanging from the thruster nozzle after pulse mode operation has produced such a state (Ref. 16).

The impurities in monopropellant grade hydrazine may also be a source of spacecraft contamination. Hydrazine purchased per MIL-P-26536C, Amendment 1, may contain up to 1% water and 0.5% aniline ($\text{C}_6\text{H}_5\text{NH}_2$) by weight as the major impurities. The greater bulk of the water apparently survives passage through the reaction zone without chemically combining with the other products to any great extent (Ref. 16); however, the formation of hydrazine hydrate ($\text{H}_2\text{NNH}_2\cdot\text{H}_2\text{O}$) has been suspected (Ref. 21). The aniline, an impurity introduced during the manufacture of the propellant, may present special contamination problems for some scientific experiments. However, the aniline can be removed by special processing (Ref. 22), and the purified propellant offers significant performance advantages, including, apparently, the elimination of the aforementioned "wash-out" phenomenon (Refs. 23,24).

The primary contaminants generated by monopropellant hydrazine thruster operation thus appear to be undecomposed hydrazine, water, and aniline, since these constituents of the exhaust products can be expected to adhere to spacecraft surfaces at temperatures above 100°K . Ammonia will begin to become an offender at temperatures slightly below this, and nitrogen will present problems only at the most extreme low temperature limits.

This report describes a series of tests to characterize the contamination potential of a low thrust monopropellant hydrazine thruster to surfaces above 100°K . This is an extension of previous investigations which mapped the plume flow field and measured the contamination which would be expected on surfaces at 223°K to 323°K (Ref. 25).

The Hamilton Standard Division of United Technologies, Inc. loaned a 0.89N thrust engine to the Air Force Rocket Propulsion Laboratory (AFRPL), and thence

to the Jet Propulsion Laboratory (JPL) for the present series of tests. The engine was installed in an ultrahigh vacuum molecular sink facility and fired vertically downward such that the exhaust plume would impinge on five quartz crystal microbalances (QCMs). The QCMs were located approximately 1.1 m below the nozzle exit plane at angles of approximately 0° , $\pm 15^\circ$, and $\pm 30^\circ$ with respect to the nozzle centerline. The QCM temperatures were controlled such that mass adhering to the crystal surface at temperatures of from 106°K to 256°K could be measured.

Thruster duty cycles of 25 ms on/5 seconds off, 100 ms on/10 seconds off, and 200 ms on/20 seconds off were investigated. The effect of water in the hydrazine was assessed by adding water to the propellant during one series of tests. The change in contaminant production with thruster life was assessed by subjecting the thruster to a 100,000 pulse aging sequence and comparing the before and after contaminant deposition rates.

II. EXPERIMENTAL FACILITY

A. Molecular Sink Vacuum Chamber

One of the major difficulties associated with the study of the far field rocket exhaust plume is the sensitivity of any mass flux measurement to gas recirculation effects within the space simulation facility. The JPL molecular sink (MOLSINK) used for the present study is an ultrahigh vacuum chamber which is capable of cryopumping injected gases at a very high rate, thus reducing the molecular scatter to a minimum.

The MOLSINK facility consists of a vacuum chamber and associated cryogenic and vacuum systems, as shown in Figure 1. The chamber itself, shown in Figure 2, encloses an inner liner and molecular trap. The inner liner is filled with liquid nitrogen and acts as a massive heat sink. The nitrogen is supplied to the inner liner from a central tank and is then vented to the atmosphere. The molecular trap, which is the innermost chamber, is a sphere approximately three meters in diameter. The aluminum walls are wedge-shaped, resembling an anechoic chamber, with a total surface area of 186 square meters. These walls are maintained at 10°K to 15°K by gaseous helium which circulates within a manifold of tubes at approximately 7°K . The helium is kept at this temperature by a refrigerator located adjacent to the chamber. The chamber walls are also coated with titanium, which acts as a "getter" material to trap any helium and hydrogen that is not cryopumped by the 10°K surfaces.

As can be seen in Figure 3, the MOLSINK chamber has two doors. The propulsion system lines and thermal control elements come through the upper door, which is a relatively small surface located in the distant backflow region of the rocket plume. The bottom door provides routine access to the chamber between tests; it is covered with a copper cone cooled with liquid nitrogen or liquid helium. The bottom door temperature can thus be controlled and the deposited frost maintained as a thin film by collecting any excess in a "cold bucket" around the cone rim.

The amount of helium and hydrogen that can be pumped is greatly increased by coating the walls with a frost of gas that has a relatively high melting

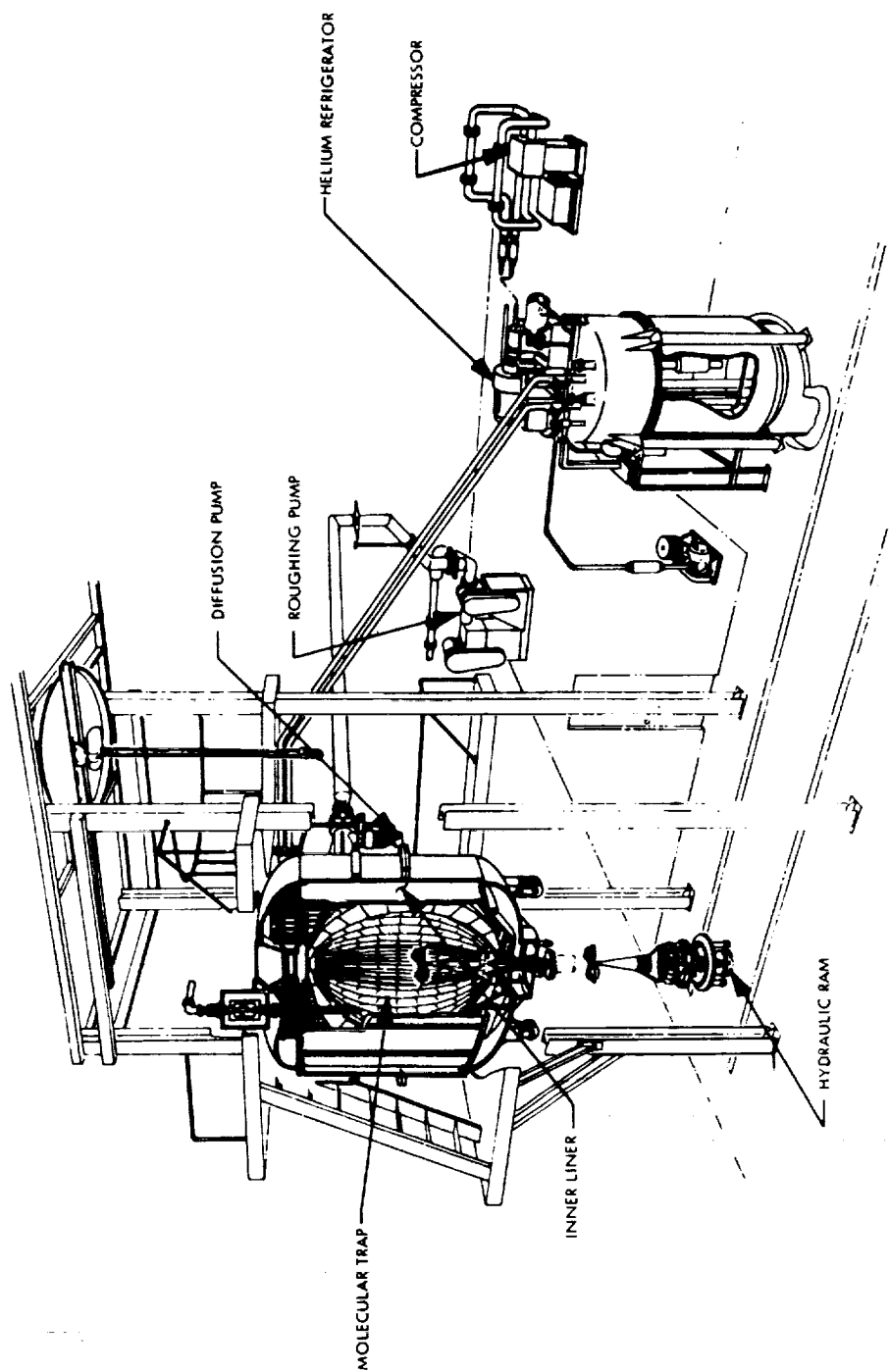


Figure 1. MOLSINK Vacuum Chamber and Auxiliary Equipment

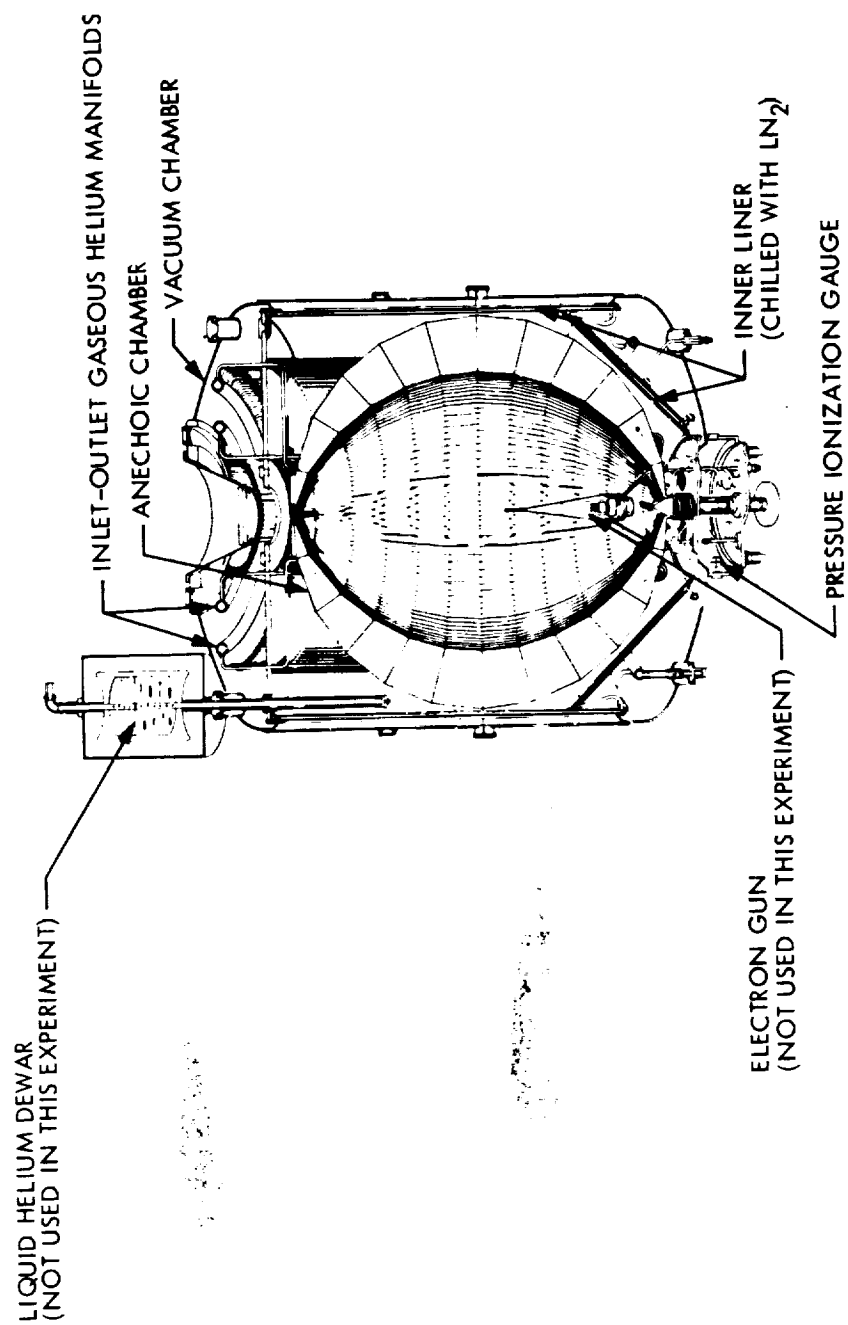


Figure 2. Molecular Sink (MOL SINK) Ultrahigh-Vacuum Chamber

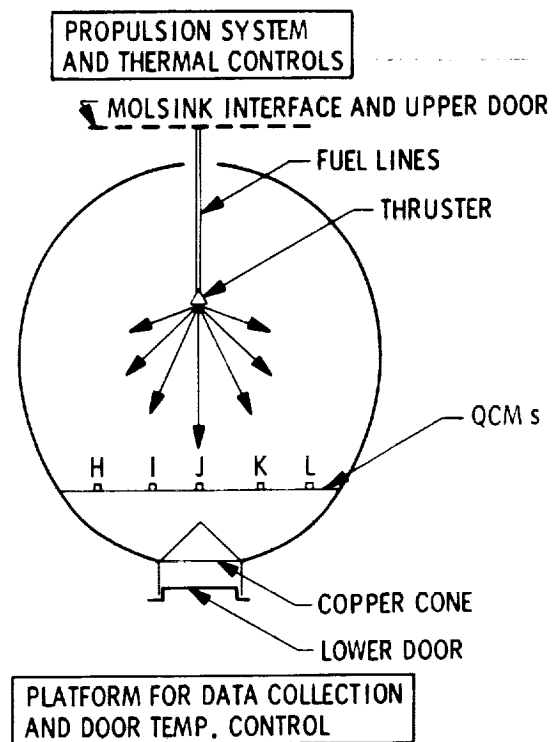


Figure 3. General Arrangement of Systems in the MOLSINK Facility (Not to Scale)

point; the frost then cryosorbs helium and hydrogen effectively. Carbon dioxide is used routinely for this purpose in MOLSINK operations. Since only a single molecular layer or so of hydrogen is cryosorbed by a frost layer, a continuous bleeding of carbon dioxide is sometimes necessary when firing a monopropellant hydrazine thruster.

The CO₂ injection system consists of a nozzle-plenum assembly located near the top of the MOLSINK chamber; it enters through the upper door. The flow of CO₂ is controlled by a solenoid valve operated by a relay which is in turn energized by a pulse generator. The pulse generator is so synchronized as to be out of phase with the thruster valve driver assembly. The CO₂ solenoid valve can also be operated manually. In order to minimize undesired contamination being introduced into the chamber, the CO₂ is supplied from a bottle and filtered first by a 20μm and then by a 1μm filter.

The carbon dioxide should condense as a solid at approximately 85°K (extrapolation of data from Ref. 26) for a nominal MOLSINK operating pressure of 10⁻⁴ Pa (7.5 x 10⁻⁷ torr). Since the minimum QCM temperature used for the present experiment was 106°K, the influence of the CO₂ injection on the QCM data was expected to be negligible. However, a separate test was conducted to measure the contribution of the CO₂ to the mass deposition rate at a crystal temperature of 144°K. The measured mass accretion due to CO₂ was found to be two orders of magnitude less than that due to thruster firing and no attempt was made to correct the data for this effect. No evidence of CO₂ accretion at the higher crystal temperatures was observed during operation of the CO₂ injection system prior to tests at these temperatures, and the sole run at a crystal temperature of 106°K was conducted without CO₂ injection.

The cryosorption rates for hydrogen and helium are highly dependent upon the wall temperature, and any process that will affect the wall temperature will result in a variation of chamber background pressure once these gases have been introduced into the chamber. During MOLSINK operation, a cryogenic environment exists within the chamber. Thermal control of such items as propellant lines and valves is necessary to prevent freezing of the propellants. These warm surfaces are protected from radiation losses by appropriate shielding, while the heat conduction losses are negligible if good insulation is used and low pressure is maintained in the chamber. If for some reason the hydrogen sorption onto the walls is diminished, any additional hydrogen injected into the chamber will reduce the vacuum, resulting in increased heat conduction losses. This causes additional warming of the walls which results in more hydrogen desorption. This phenomenon exhibits exponential growth which results in the desorption of hydrogen from the walls within a matter of seconds; it is hereafter referred to as the "avalanche" effect.

Additional information concerning the design of the MOLSINK facility may be found in References 27 and 28.

B. Microbalance Instrumentation

Five quartz crystal microbalances (QCMs) were used to measure the contaminant mass deposition from the rocket exhaust plume.

The heart of the QCM is a quartz crystal, the piezoelectric effect of which is used to stabilize the resonant frequency of an electronic oscillator. The resulting resonant frequency depends upon several parameters, but if the oscillator circuit constants and polarization voltages are fixed, the specific modes of vibration will depend only upon the orientation of the cut plane with respect to the crystal axes. For a given cut angle, the precise resonant frequency will depend upon the temperature and the amount of mass which is deposited on the crystal surface. If the crystal experiences a variation in temperature ΔT and a mass variation Δm , the resulting frequency shift Δf can be expressed as:

$$\Delta f = C_m \Delta m + C_T \Delta T$$

where C_m and C_T are the mass and temperature coefficients, respectively, of the crystal.

In general, both C_m and C_T are functions of temperature and cut angle. However, for a considerable change in temperature and cut angle, the mass coefficient does not vary by more than 5% and can be assumed a constant. If a cut angle is chosen such that C_T can be set to zero over some temperature range, then the frequency shift is proportional only to the mass deposited on the crystal surface, and the crystal can be used as a delicate microbalance for measuring small masses.

The crystals selected for use in the present experiment were AT cuts (Ref. 29) which vibrate in the thickness shear mode at approximately 5 MHz. An illustration of the crystal, showing the electrodes and the mode of vibration, is presented in Figure 4. The precise AT cut for crystals H, I, K, and L (see Figure 3) was $35^\circ 10'$, while the cut for crystal J was $40^\circ 28'$. The $40^\circ 28'$ cut has a small temperature coefficient at temperatures of $10^\circ K$ to $125^\circ K$, while the $35^\circ 10'$ cut has a minimum temperature coefficient over the range $125^\circ K$ and above. By proper QCM design, the effects of temperature can be reduced still further. Bartera (Ref. 30) has produced a design which is simple yet provides a very efficient temperature compensation. This arrangement is shown in Figure 5. A doublet crystal plate is cut and polished; gold electrodes are deposited on one side, as shown in Figure 6, while a common rectangular electrode is used on the other side. If the crystal is driven at low voltage, each half of the doublet will oscillate independently. By protecting one half from mass deposit with a screen which is optically thin to the radiation environment, the beat frequency between the two halves, which have achieved the same equilibrium temperature, can be easily correlated with the mass deposited on one half. The temperature compensation thus achieved renders negligible the effect of temperature on the QCMs over the range of temperature covered in the present experiment. The change in beat frequency ΔF can thus be related to deposited mass by the simple relation:

$$\Delta m = (1/C_m) \Delta F$$

A derivation of the above relation and C_m is given in Appendix A.

The design of a QCM is very dependent upon the intended application, including the environment and operating conditions under which it will be required to function. When investigating rocket exhaust contaminant distribu-

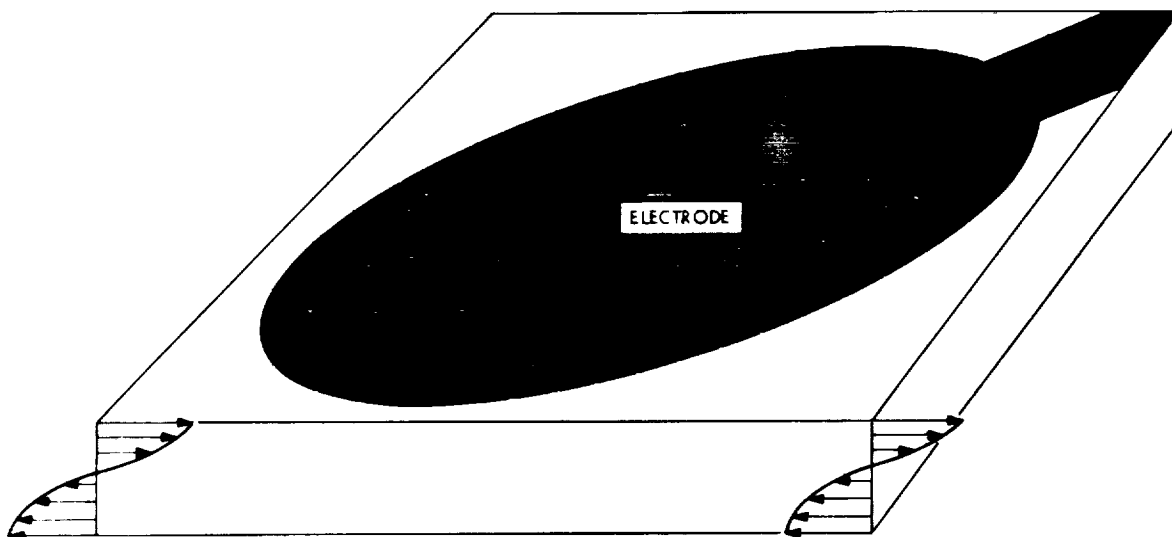


Figure 4. Quartz Crystal Electrodes and Demonstration of the Thickness Vibration Mode

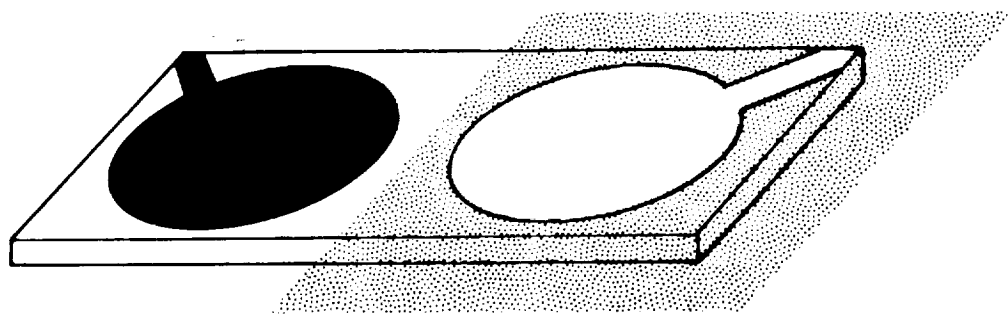
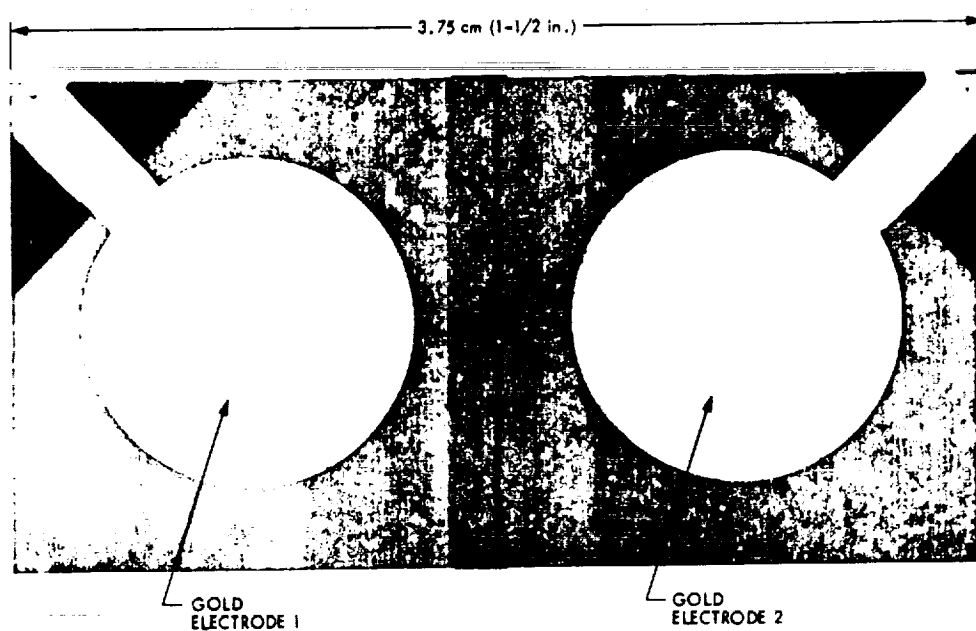
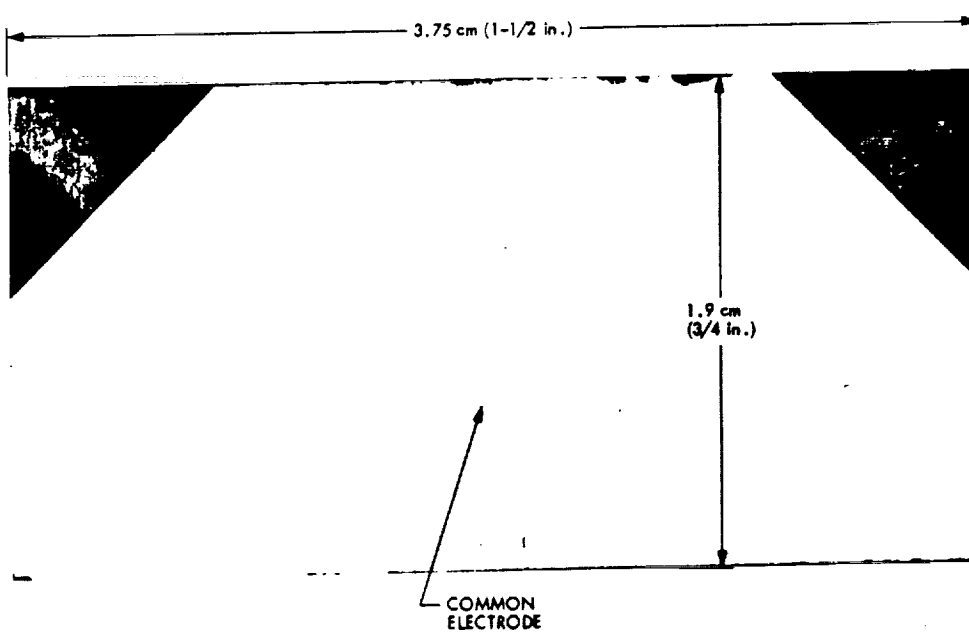


Figure 5. Doublet QCM



Side 1: Independent Electrodes



Side 2: Common Electrode

Figure 6. Quartz Crystal Doublet

tion, one is interested in setting the QCM sensing surface at a constant temperature within a specified range. Since the experimenter does not necessarily know in advance the condensation temperature of all the contaminants from a monopropellant hydrazine thruster, the QCM must have the capability of operating over a temperature range from NH_3 condensation to room temperature. In order to selectively sample the contaminants by cryotrapping on the crystal surface, the QCM is exposed to the plume and its frequency output is monitored while it is operated at various constant temperatures.

Each QCM unit was equipped with heaters which were controlled by a copper-constantan thermocouple located in the proximity of one of the heaters, while the crystal temperature was monitored by a similar thermocouple placed on one corner of the crystal. The heater-controlling thermocouples of the variable temperature QCMs dynamically maintained the temperature of the units. The actual setting of the control point for these heaters was determined by the thermocouple located on the crystal.

The crystal itself is mounted to an aluminum block by a set of "hairbrush" gold wires, as shown in Figure 7, which are attached to the common electrode by a high thermal conductivity, low outgassing silver epoxy. The gold wires provide a good thermally conducting path between crystal and block while precluding the development of any potentially damaging thermal stresses within the crystal. Two gold wires connect the crystal electrodes to two heat sinks, which are in turn connected to the electronics package. The unit is covered with a Teflon block collimator provided with two circular apertures, one of which is covered with a transparent piece of Mylar. A photograph showing the crystal doublet, heaters, and collimator is presented as Figure 8. A view of the QCMs from the position of the thruster nozzle (looking downward) is given in Figure 9. All the materials used in QCM construction, mounting, and wiring were selected to minimize outgassing rates in vacuum. The electronics and heater wiring from all the QCM units was extracted through the bottom MOLSINK door and routed to the data acquisition system.

C. Propulsion System

An REA 10-18 thruster/valve assembly was loaned for the present experiment by Hamilton Standard Division, United Technologies, Inc. The nominal characteristics of this thruster are summarized in Table I.

TABLE I. Nominal Characteristics of Hamilton Standard REA 10-18 Thruster

Steady State Thrust	0.89N (0.2 lbf)
Steady State Inlet Pressure	1.62×10^6 Pa (235 psia)
Steady State Chamber Pressure	1.14×10^6 Pa (165 psia)
Catalyst	Shell 405
Nozzle Area Ratio	55:1
Valve Manufacturer	Wright

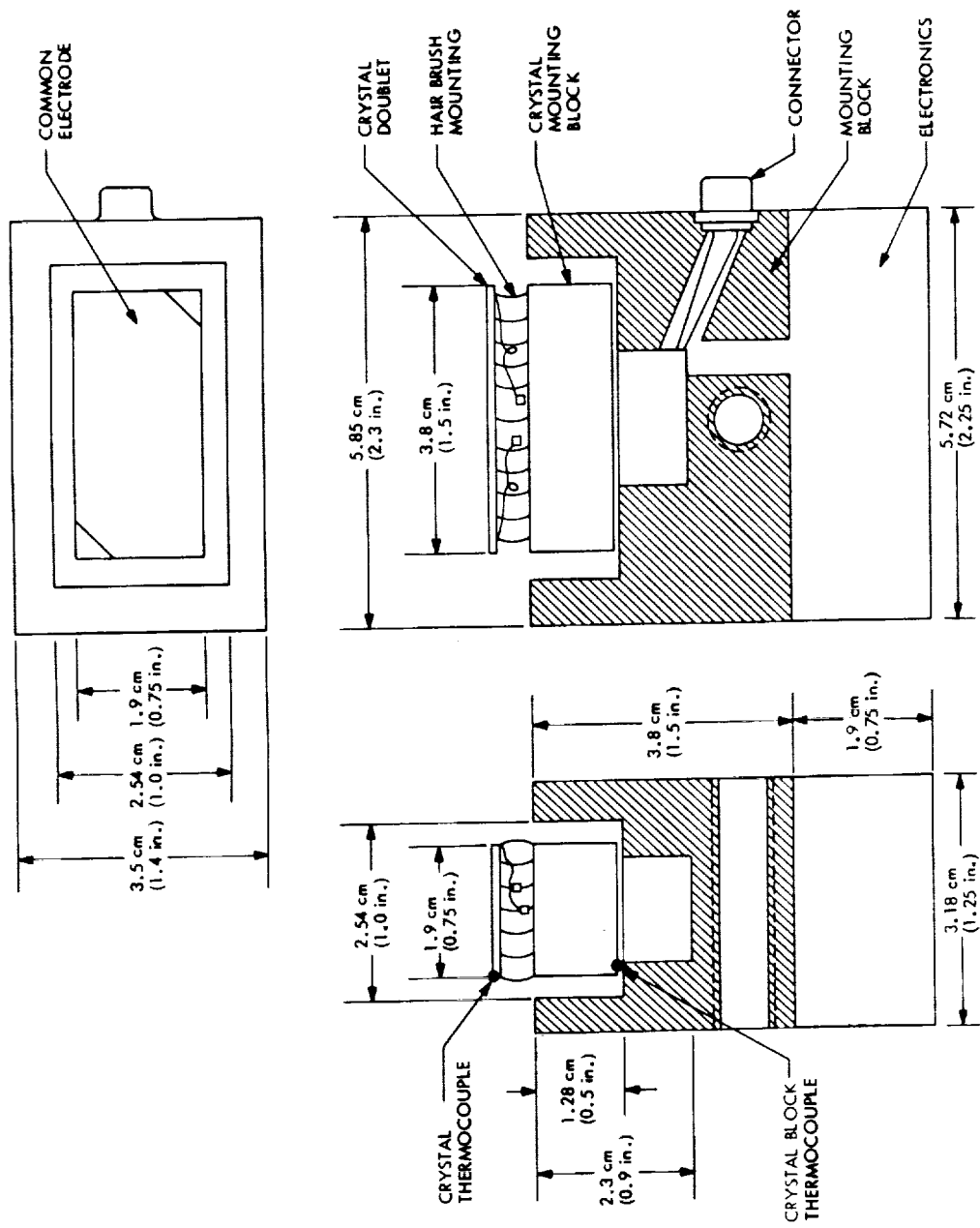


Figure 7. Schematic Diagram of a Variable Temperature QCM Unit

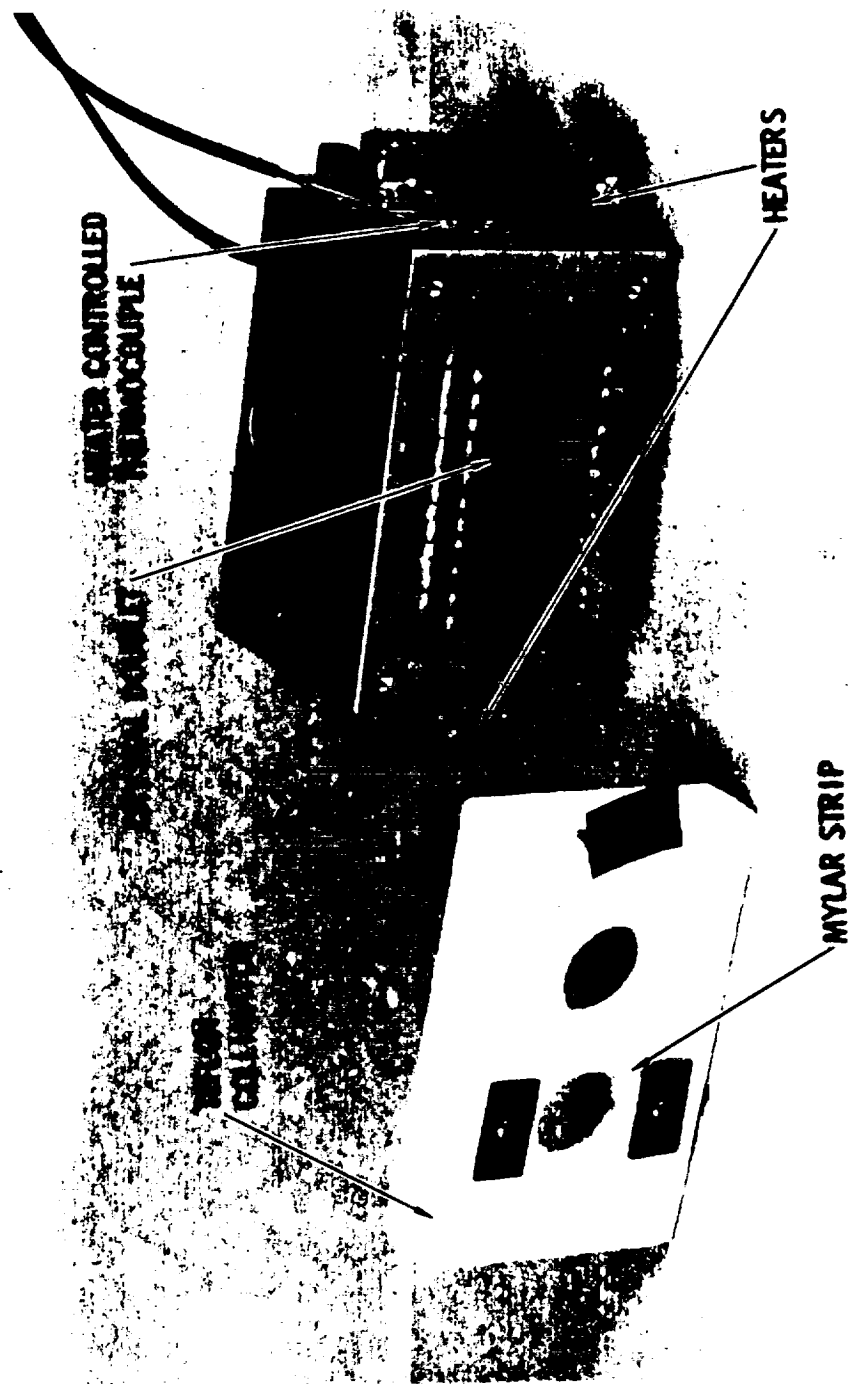


Figure 8. A View of a QCM Unit With the Teflon Collimator Removed

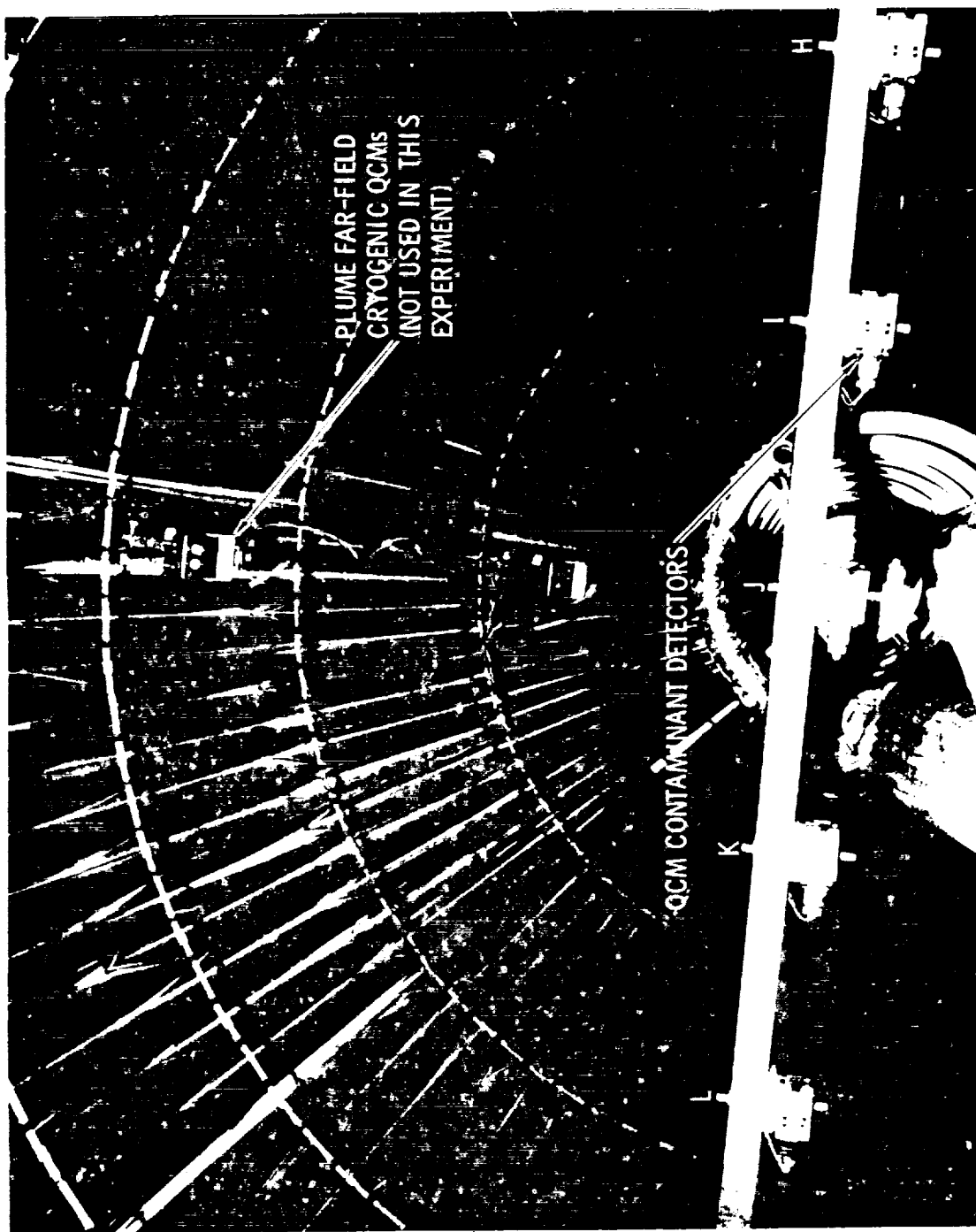


Figure 9. QCMs as Viewed From the Thruster

The thruster had been subjected to 2353 pulse mode firings and 292 seconds of steady state firing prior to installation and testing in the MOLSINK facility. The engine was located at the axis of the chamber with the nozzle exit 64.67 cm from the top of the chamber as shown in Figure 10. It was mounted on a vertical bracket supported by a horizontal bar, and visually aligned to fire vertically downward towards the five QCMs. The propellant lines were passed through the upper door and thence to the propellant feed module. A photograph of the thruster as installed in the MOLSINK is presented as Figure 11.

The thruster/valve assembly and propellant line were inside the cryogenic environment of the chamber and thus required protection from freezing. This protection was afforded by strip and spot heaters and radiation shielding. The propellant line temperature was monitored by a series of thermocouples distributed along the line. These thermocouples controlled several low outgassing Kapton film heaters (manufactured by Electrofilm, Inc.) which were wrapped around an aluminum tube as shown in Figure 12. The thermocouple cabling, hydrazine propellant line, and a gaseous nitrogen purge line shared the controlled environment within the aluminum tube.

Maximum thermal insulation was utilized for all components to minimize heat leaks to the MOLSINK chamber walls. The aluminum tube and thruster valve were covered by aluminum foil in order to prevent excessive radiation losses.

The engine and valve were instrumented with several thermocouples and a coiled coaxial electrical heater. This arrangement provided thermal control of the engine catalyst bed and allowed the throat and catalyst bed temperature to be monitored. Heater wiring and solenoid valve cabling were collected between the aluminum tubing and the aluminum foil wrapping. They were extracted from the chamber by feed-throughs located at the top door of the MOLSINK.

The nominal temperatures of the thermally controlled components are given in Table II.

TABLE II. Nominal Temperatures of Thermally Controlled Components

COMPONENT	TEMPERATURE
Fuel Lines	293-303°K (67-85°F)
Filter	292-303°K (67-85°F)
Solenoid Valve	293-303°K (67-85°F)
Catalyst Bed	480°K (400°F)

The propellant feed module was located at the top of the MOLSINK chamber outside the upper door. The module included the gaseous nitrogen purge system, the hydrazine propellant supply tank, a piston flow meter, and instrumentation for monitoring the propellant temperature and pressure. The piston flowmeter was calibrated and incorporated into the propulsion module so that the mass deposition rate as measured by the QCMs could be related to the propellant

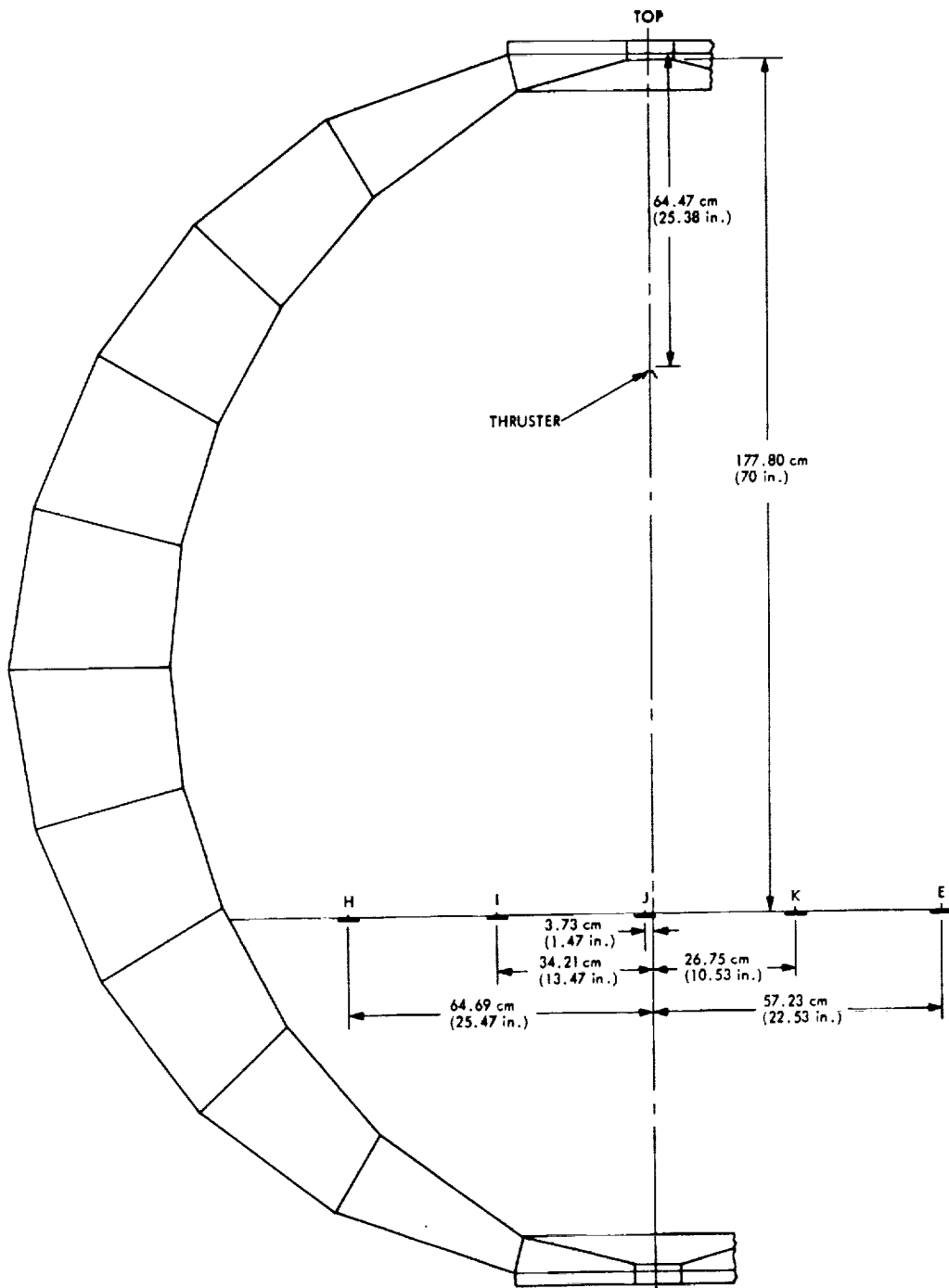


Figure 10. QCM Orientation and Thruster Position in MOLSINK Chamber



Figure 11. Hamilton Standard REA 10-18 Thruster as Installed in MOLSINK Facility (Heat Shield Removed)

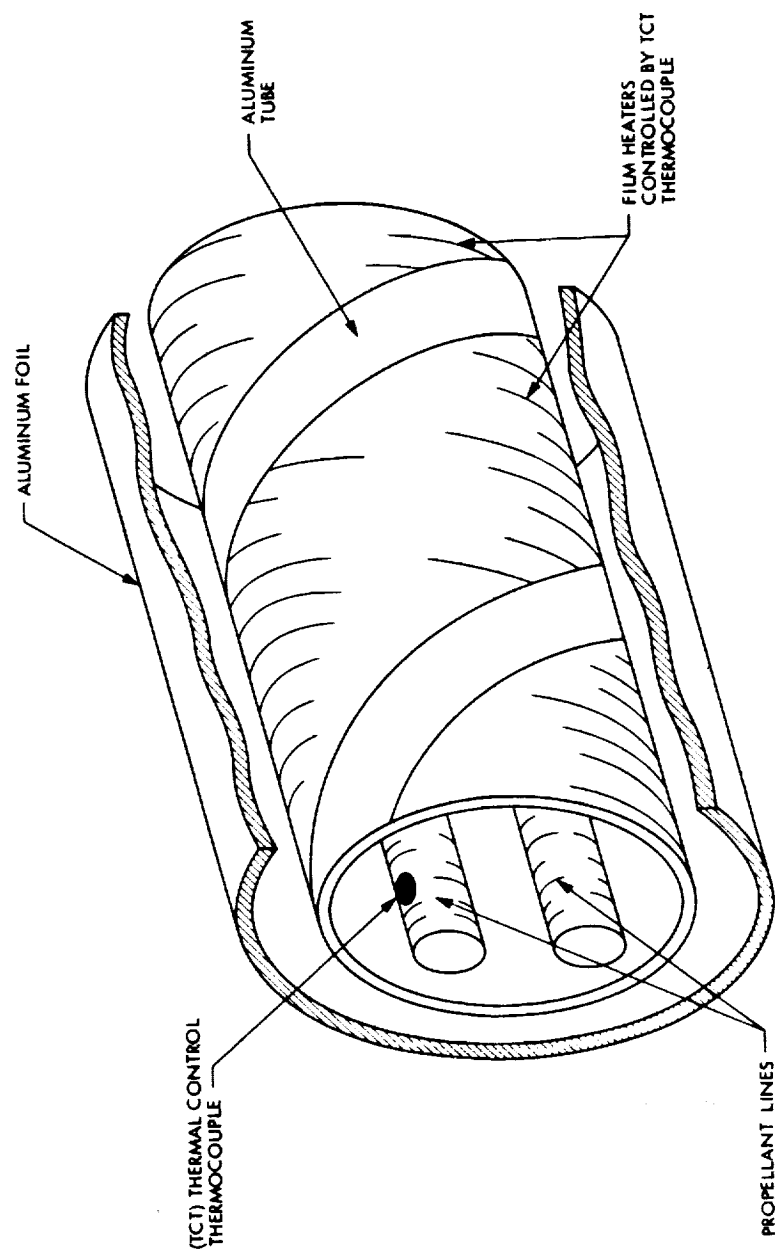


Figure 12. Thermal Control System for Propellant Lines

flowrate through the thruster. A schematic diagram of the propulsion module and those components that were located within the MOLSINK chamber is shown in Figure 13. The propellant was introduced to the thruster through valve VFL-1, filling both lines with hydrazine from the solenoid valve to valve VPG-1. The line containing VPG-1 is the gaseous nitrogen purge.

Operation of the propellant system was commanded by remote control from the lower floor of the MOLSINK facility after the propellant tank had been pressurized. A variable pulse width and variable pulse separation sequence timer system was used to control thruster firing.

The thruster chamber pressure tap was closed off during the contamination testing and its volume was minimized by positioning a needle in the line cavity. During the aging sequence only, a Statham Model PA856 pressure transducer and approximately four inches of 1/16 inch outside diameter connecting tubing were attached to the tap for the purpose of monitoring engine performance.

D. Data Acquisition System

Two separate data acquisition systems were used for this experiment. The primary system was a digital data acquisition system which swept a total of 59 channels and printed out a permanent record of all readings plus the time. The majority of these channels was dedicated to the instrumentation which provided thermal control for the prevention of freezing of the components within the MOLSINK chamber; these will not be further discussed. Fourteen of the sampled channels have a direct bearing on the experiment and thruster performance. These channels include the five QCM frequencies, the five crystal temperatures, propellant inlet pressure, propellant inlet temperature, position of the linear variable potentiometer of the piston flowmeter, and thruster chamber temperature.

Digital sampling intervals of 88 and 134 seconds were utilized, which correspond to anywhere from 4 to 26 pulses fired between samples, depending upon the duty cycle.

The printed output from the primary data system was punched onto computer cards and used exclusively for the subsequent data reduction and analysis.

The signals from each of the QCMs were also split and routed through an oscilloscope and a digital counter, and then through a digital-to-analog converter to strip charts so that a real time evaluation of the mass deposition rate data could be made. The crystal and critical thruster temperatures were also displayed in real time on strip chart recorders, as was the background vacuum pressure in the MOLSINK chamber.

E. Facility Operation

All thermal controls were set to nominal temperatures, and the chamber doors were closed. A mechanical pump reduced the chamber to 1.33×10^{-1} Pa (10^{-3} torr), and a diffusion pump brought it down to 1.33×10^{-3} Pa (10^{-5} torr). After leak checking, liquid nitrogen was introduced into the inner liner of the chamber. That brought the temperature of the liner and molecular trap to 80°K at the end



Figure 13. Hydrazine Propellant Module Flow System Schematic Diagram

of 24 hours. At this point, with the pressure still at 1.33×10^{-3} Pa (10^{-5} torr), the helium refrigerator was started. At the end of eight hours, the molecular trap temperature had dropped to 10°K , and the chamber pressure had reached a low of 1.33×10^{-7} Pa (10^{-9} torr). At this point the facility was at its nominal high-vacuum operating mode, and the calibration and test procedures were initiated. The systems were checked by flowing gases through the auxiliary CO_2 injection system nozzle, and several runs on the data system were conducted until all systems were debugged, coordinated, and properly interfaced.

III. TEST DESCRIPTION

The matrix of thruster operating conditions and crystal temperatures for the tests reported herein are given in Table III. The nominal thruster propellant inlet pressure for all test runs was 790 kPa (100 psig), which corresponds to a steady state thrust of 0.4N (0.09 lbf). The initial catalyst bed temperature was 480°K (400°F), and the propellant inlet temperature was approximately 300°K (80°F).

Runs 1, 2, and 3 represent baseline testing at crystal temperatures of 200°K , 172°K , and 144°K . The baseline thruster duty cycle was 100 ms on, 10 seconds off.

After run 3 the failure of the catalyst bed heater was discovered. It was replaced by a coiled resistance heater which required removing and discarding the thruster heat shield. Though the initial catalyst bed temperature could be maintained at 480°K (400°F), the additional radiative heat loss resulted in approximately a 45°K (80°F) reduction in the equilibrium temperature achieved in the catalyst bed at the baseline duty cycle.

Tests 4 and 5 were high rate pulse trains at a thruster duty cycle of 25 ms on and 5 seconds off at crystal temperatures of 172°K and 144°K .

Runs 6 through 10 were low rate pulse trains at a duty cycle of 200 ms on and 20 seconds off. Runs 6 and 7 were conducted for the purpose of measuring the mass deposition rate at this duty cycle for crystal temperatures of 172°K and 144°K . Runs 8, 9, and 10 represent an attempt to characterize the contaminant production of the engine for the first pulses of a train, during which time the catalyst bed temperature is rising towards its equilibrium value. During runs 7, 8, 9, and 10 data were acquired digitally after approximately every fourth thruster pulse.

Run 11 is a rebaseline test at a crystal temperature of 144°K . Run 12 is a baseline measurement at a crystal temperature of 106°K .

The hydrazine propellant used in this experiment was purchased per MIL-P-26536C, Amendment 1. An assay of this propellant determined that it contained 0.71% H_2O by weight. For tests 13 and 14 the amount of water in the propellant was increased to 1.8% in order to assess the difference this would make on the contamination measurements at crystal temperatures of 172°K and 144°K .

At the conclusion of the water addition tests, the propulsion system was purged and propellant from the original stock was loaded. With the MOLSINK at

Table III. Test Sequence

Run Number	Duty Cycle (ms on/sec off)	Crystal Temperature ($^{\circ}$ K)	Pulses Per Run	Cumulative Pulses At Beginning of Test	Purpose of Test
1	100/10	200.	1000.	3353.	Baseline Testing
2	100/10	172.	1000.	4353.	
3	100/10	144.	334.	5353.	
4	25/5	172.	2222.	6682.	High Rate Pulse Train
5	25/5	144.	2059.	13687.	
6	200/20	172.	410.	17951.	Low Rate Pulse Train
7	200/20	144.	60.	19441.	
8	200/20	144.	60.	19860.	
9	200/20	144.	60.	19920.	
10	200/20	144.	60.	19980.	
11	100/10	144.	750.	23780.	Baseline
12	100/10	106.	302.	26349.	Testing
13	100/10	144.	782.	27785.	Water
14	100/10	172.	767.	28927.	Addition
Aging Sequence (See Table IV)					
15	100/10	172.	940.	131011.	Baseline Testing
16	100/10	200.	990.	132221.	
17	100/10	144.	1024.	134001.	

1.33×10^{-1} Pa (10^{-3} torr) and at ambient temperature, the thruster was subjected to an aging sequence of 100,275 pulses; these were accrued by repeating three times the test sequence shown in Table IV. At the conclusion of the aging sequence, the MOLSINK was returned to its high-vacuum, low temperature operating condition and baseline tests at crystal temperatures of 200°K, 172°K, and 144°K were conducted to ascertain whether or not the effects of thruster life had an influence on the contaminant production. These baseline tests were runs 15, 16, and 17.

An examination of the cumulative pulses column of Table III will reveal that much testing took place that is not reported here. This testing included runs at crystal temperatures of 256°K, for which no mass deposition was recorded, and runs at 228°K, for which either no mass deposition was recorded or the results were uninterpretable due to scatter. This will be further discussed in Section IV.

With the exception of runs 8, 9, and 10, all the tests reported here were of several thousand seconds duration. As has been previously explained, these three tests were an attempt to measure a transient phenomenon and were thus of only approximately 1200 seconds duration. Many additional short tests of this nature were conducted; they were, however, inadvertently conducted at the lower digital sampling rate, allowing 133 seconds to elapse between readings. They were also primarily conducted at crystal temperatures of 172°K in an attempt to detect undecomposed hydrazine without condensing any ammonia. Data at this and higher temperatures were very difficult to interpret due to scatter in the very low measured mass deposition rates and required long test runs to establish the frequency trend.

A considerable effort was put forth in an attempt to extract useful results from the short tests, including a least squares fitting of both linear and cubic relations to the data (see Appendix B). Unfortunately, use of the QCM technique requires that an evaluation of the time rate of change of crystal frequency be made, and the differentiation process which must necessarily be applied to the data tends to exaggerate uncertainties. Because no consistent results could be obtained from the few data points of the short runs, and since the elapsed time between data samples was so great as to miss most of the transient phenomenon anyway, these runs were discarded and will not be subject to further analysis or discussion.

IV. RESULTS

The results from each of the tests described in Section III are summarized in Table V. The mass deposition rate recorded by each crystal has been converted to mass deposition rate per unit solid angle, gm/sec/steradian, so that a comparison among the five crystals can be more easily made. Where a value is not given, the data indicated a mass deposition rate either too low to be reliably determined or the data scatter was such as to render the result uninterpretable. As described in Section III, runs 8, 9, and 10 were short runs for the purpose of characterizing the contaminants produced by the thruster during the first few pulses. The mass deposition rates shown in Table V for these three runs were obtained from a curvefit to the data and are representative of the contamination production at the beginning of the pulse train.

Table IV. Thruster Aging Sequence
(Repeated Three Times)

Duty Cycle (Seconds)		Number of Pulses	Time Elapsed (Seconds)	Total On-Time (Seconds)
on	off			
0.020	120	50	6001.0	1.00
0.035	120	50	6001.75	1.75
0.050	120	50	6002.50	2.50
0.100	120	50	6005.00	5.00
0.250	300	5	1501.25	1.25
0.015	15	100	1501.50	1.50
0.500	120	10	1205.00	5.00
1.0	120	10	1210.00	10.00
0.125	12.375	1000	12500.00	125.00
0.04	1.16	5000	6000.00	200.00
0.04	0.40	7000	3080.00	280.00
1.0	10.0	100	1100.00	100.00
0.10	0.900	6000	6000.00	600.00
0.075	0.525	6000	3600.00	450.00
0.090	0.100	7000	1330.00	630.0
0.020	0.020	1000	40.00	20.0
Subtotal:		33425	63078	2433
Total for Aging Sequence:		100275	189234	7299

Table V. Summary of Results

Run Number	Average Propellant Flowrate (gm/sec x 10 ³)	Equilibrium Chamber Temperature (°K)	Mass Deposition Rates Per Unit Solid Angle (gm/sec/sr)				
			H	I	J	K	L
1	2.99	794.	2.00 X 10 ⁻⁷	5.25 X 10 ⁻⁸	9.00 X 10 ⁻⁷	1.69 X 10 ⁻⁷	6.07 X 10 ⁻⁷
2	2.92	786.	---	4.48 X 10 ⁻⁷	1.23 X 10 ⁻⁶	2.03 X 10 ⁻⁷	7.57 X 10 ⁻⁷
3	2.99	783.	1.26 X 10 ⁻⁵	5.39 X 10 ⁻⁵	5.86 X 10 ⁻⁵	5.49 X 10 ⁻⁵	---
4	2.01	673.	---	1.75 X 10 ⁻⁷	4.39 X 10 ⁻⁷	---	---
5	1.978	689.	6.43 X 10 ⁻⁶	3.28 X 10 ⁻⁵	3.11 X 10 ⁻⁵	2.68 X 10 ⁻⁵	2.47 X 10 ⁻⁶
6	2.71	719.	---	4.20 X 10 ⁻⁷	1.83 X 10 ⁻⁶	5.42 X 10 ⁻⁷	4.03 X 10 ⁻⁷
7	2.811	713.	6.33 X 10 ⁻⁶	3.05 X 10 ⁻⁵	3.90 X 10 ⁻⁵	3.33 X 10 ⁻⁵	2.09 X 10 ⁻⁶
8	2.792	---	1.28 X 10 ⁻⁵	4.62 X 10 ⁻⁶	4.88 X 10 ⁻⁵	4.07 X 10 ⁻⁵	1.42 X 10 ⁻⁵
9	2.750	---	1.26 X 10 ⁻⁵	5.04 X 10 ⁻⁵	5.24 X 10 ⁻⁵	4.46 X 10 ⁻⁵	2.81 X 10 ⁻⁵
10	2.565	---	1.01 X 10 ⁻⁵	6.85 X 10 ⁻⁵	5.53 X 10 ⁻⁵	1.01 X 10 ⁻⁵	1.35 X 10 ⁻⁵
11	---	741.	1.14 X 10 ⁻⁵	4.48 X 10 ⁻⁵	4.31 X 10 ⁻⁵	3.52 X 10 ⁻⁵	2.66 X 10 ⁻⁶
12	---	736.	4.77 X 10 ⁻⁴	8.69 X 10 ⁻⁴	1.20 X 10 ⁻³	2.03 X 10 ⁻⁴	1.42 X 10 ⁻⁴
13	---	733.	1.39 X 10 ⁻⁵	6.32 X 10 ⁻⁵	6.62 X 10 ⁻⁵	5.99 X 10 ⁻⁵	4.61 X 10 ⁻⁶
14	2.905	733.	2.89 X 10 ⁻⁷	9.25 X 10 ⁻⁷	1.72 X 10 ⁻⁶	4.12 X 10 ⁻⁷	---
15	2.10	706.	2.30 X 10 ⁻⁷	1.33 X 10 ⁻⁶	1.72 X 10 ⁻⁶	1.21 X 10 ⁻⁶	---
16	2.187	703.	2.72 X 10 ⁻⁷	9.53 X 10 ⁻⁷	1.02 X 10 ⁻⁶	8.58 X 10 ⁻⁷	6.45 X 10 ⁻⁸
17	2.146	700.	3.83 X 10 ⁻⁶	1.93 X 10 ⁻⁵	2.26 X 10 ⁻⁵	1.63 X 10 ⁻⁵	3.22 X 10 ⁻⁷

The propellant mass flowrate is given for all runs except 11, 12, and 13, for which the piston flowmeter was not used. The equilibrium catalyst bed temperature is shown for all runs except the short transients, 8, 9, and 10.

A. Plume Shape and Data Interpretation

The contamination results from all runs conducted prior to the aging sequence, excluding runs 8, 9, 10, 12, 13, and 14, are plotted in non-dimensionalized fashion in Figure 14. The mass flux per unit solid angle at each crystal location is divided by the value obtained from crystal J. The results from QCM J were almost always easier to interpret due to the higher mass flux at this location, and this QCM performed repeatedly well at all temperatures. This method of presentation thus allows a comparison to be made among the five QCM readings.

Several interesting observations may be made from an examination of Figure 14. The scatter in the data taken at a QCM temperature of 172°K is indicative of the difficulty that was encountered in evaluating the slope of the frequency-time curve at this and higher temperatures. This is further demonstrated by the fact that only one run at 200°K provided sufficiently consistent results to be interpretable as having evidenced any mass deposition at all prior to the aging sequence. Several times after the completion of the 172°K runs a desorption of mass from the crystals could be seen, and failure to reach a deposition/desorption equilibrium in a uniform manner on all the crystals during a run is possibly responsible for most of the scatter at crystal temperatures of 172°K and 200°K.

An additional phenomenon which probably contributed to the scatter at all temperatures may be seen by examining the results from runs conducted at crystal temperatures of 144°K. The frequency-time data at this temperature were very repeatable, and the data were almost always easily and reliably interpretable. The scatter at this temperature is primarily due to a skewness of the rocket exhaust plume, with greater mass flux being recorded on QCMs H and I than on QCMs K and L. Note that the mass flux at crystal H is always higher than that at crystal L, even though L is located closer to the nozzle centerline. For two of the five runs plotted in Figure 14c, QCM L recorded no mass deposition. A similar comparison of I and K may also be made--in fact QCM I twice recorded higher mass flux than the centerline QCM J. Though the plume was always unsymmetrical to some extent, the amount varied from run to run and no correlation with thruster geometric features or alignment is evident.

The solid line drawn through the data on Figure 14c is based upon the plume expansion approximation of Hill and Draper (Ref. 31). This formulation is based upon inviscid plume expansion correlations and will be assumed to be applicable for the core flow measurements considered here. Their relationship takes the form:

$$\frac{\left(\frac{dm}{d\Omega}\right)_{\theta}}{\left(\frac{dm}{d\Omega}\right)_{\theta=0}} = e^{-\delta^2(1-\cos \theta)^2}$$

where $\left(\frac{dm}{d\Omega}\right)_{\theta}$ is the mass flux per unit solid angle Ω at angle θ from the nozzle centerline, $\left(\frac{dm}{d\Omega}\right)_{\theta=0}$ is the mass flux per unit solid angle at the centerline,

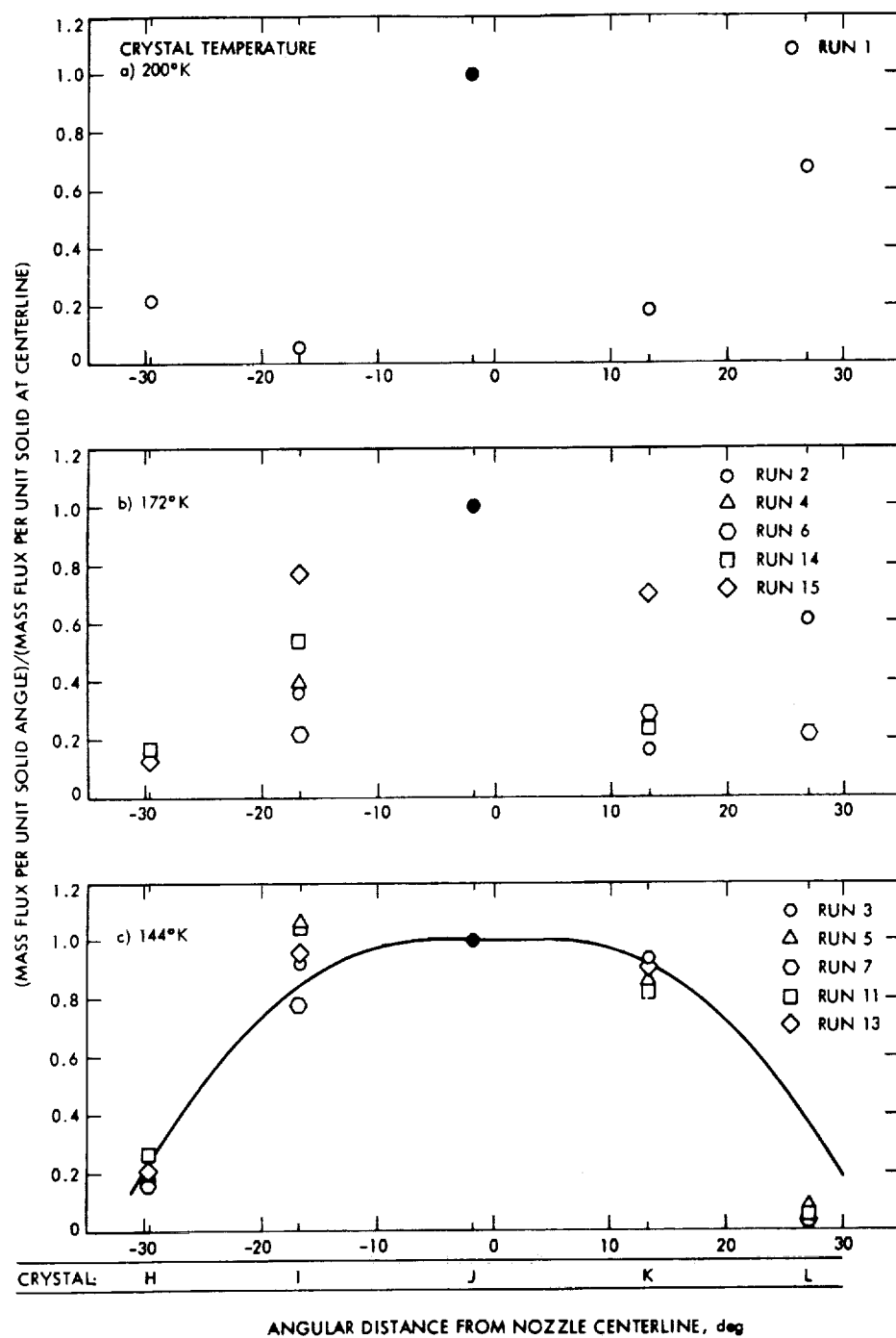


Figure 14. Measurement Repeatability Relative to Center Crystal

and δ is a plume expansion parameter. Measurements from QCMs H, I, and J for all runs conducted at a crystal temperature of 144°K were fit to the above relationship to determine the plume expansion parameter δ . Only the measurements from H, I, and J were used so that the maximum plume spreading would be achieved, thus yielding a reasonably conservative value of δ for off-axis contamination assessment. A value of $\delta = 9.59$ provides the best fit to the data in the least squares sense and was used to plot the curve shown in Figure 14c.

Hill and Draper define δ by the following relationship:

$$\delta = \left[\sqrt{\pi} (1 - C_f/C_{fm}) \right]^{-1}$$

where C_f is the actual thrust coefficient and C_{fm} is the maximum theoretical thrust coefficient. The ratio C_f/C_{fm} can be computed based upon isentropic, ideal gas relations if the nozzle expansion area ratio (55:1) the nozzle divergence half angle (15°), and the ratio of specific heats, γ , are known. Taking $\delta = 9.59$ and backing out the ratio of specific heats yields a value of $\gamma = 1.41$ for the present thruster. This is the value of γ which would be obtained at a gas temperature of 167°K for 65.5% ammonia dissociation. This would seem to indicate that for monopropellant plume expansion calculations using the Hill and Draper approximation the ratio of specific heats should be evaluated at a temperature well below that of the adiabatic reaction temperature (which is often used) and preferably near the nozzle exit temperature. Evaluation of γ at the higher temperature will, however, predict more plume spreading and thus may be more conservative for some contamination studies.

The mass flux per unit solid angle at the nozzle centerline can be calculated using the simple relationship:

$$\left. \frac{dm}{d\Omega} \right|_{\theta=0} = \delta \dot{m}_T \pi^{-3/2}$$

where \dot{m}_T is the total propellant mass flowrate to the thruster. In subsequent sections it will be desirable to remove the effects of propellant flowrate from the results. This will be done by dividing the measured centerline (QCM J) contamination by $\delta \dot{m}_T / \pi^{3/2}$, where $\delta = 9.59$, and \dot{m}_T will be as measured by the piston flowmeter for the particular run involved. The result will be called the normalized mass deposition rate and can be interpreted as the fraction of the total mass flux at the centerline which is deposited on the crystal surface.

B. Contaminant Capture as a Function of Surface Temperature

The mass deposition rate per unit solid angle for the centerline QCM J is plotted as a function of crystal temperature in Figure 15. All runs are included in this plot except the short transient runs 8, 9, and 10.

At crystal temperatures of 172°K and 200°K a mass deposition rate of approximately 10^{-6} gm/sec/sr is indicated. As previously discussed, desorption from the crystals was noted at the conclusion (i.e., after the thruster was stopped) of several of the runs at crystal temperatures of 172°K and higher.

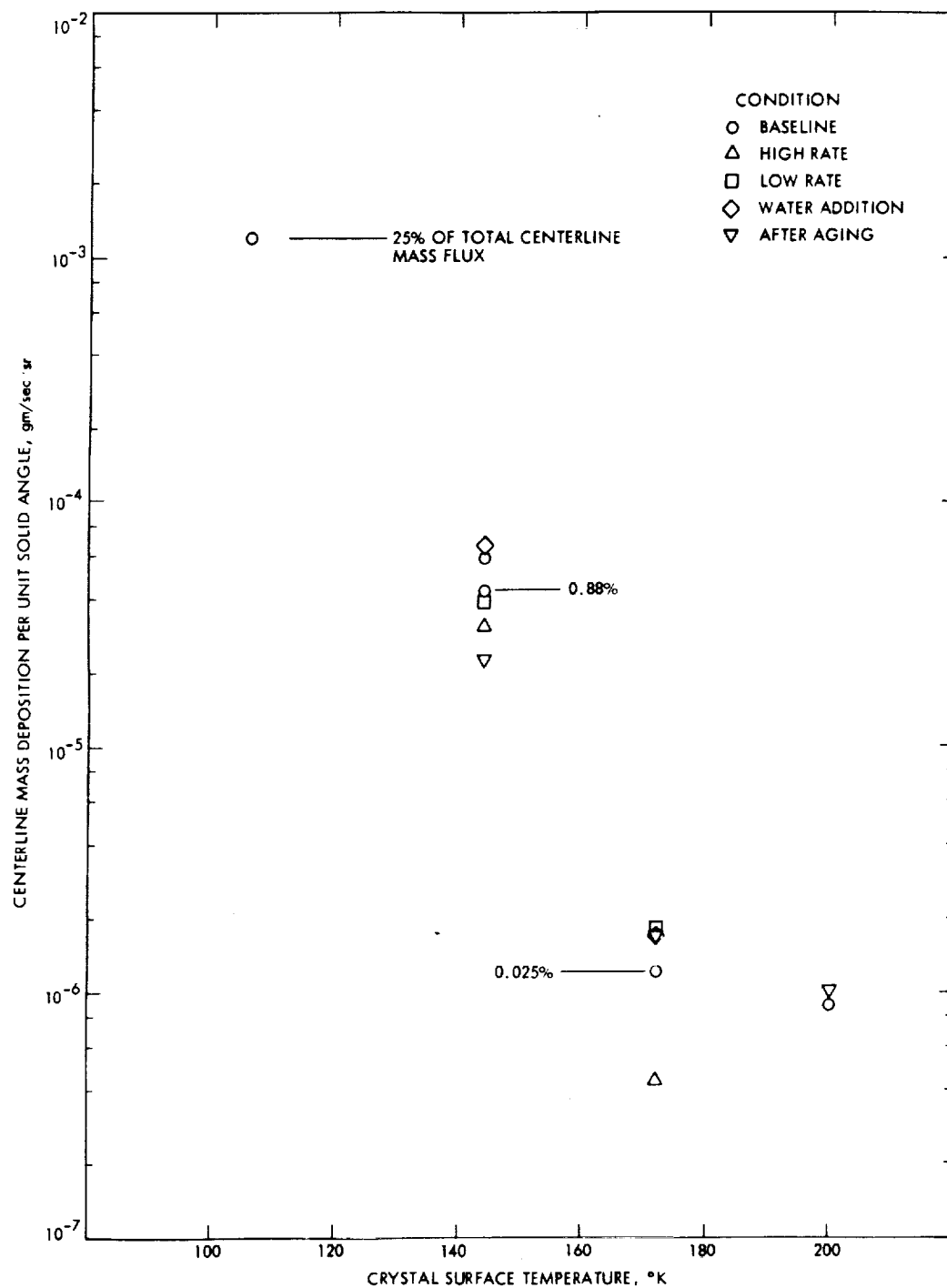


Figure 15. Effect of QCM Crystal Temperature on Centerline Mass Deposition Rate

For a crystal temperature of 144°K the mass deposition rate is over an order of magnitude greater than that recorded at 172°K . This abrupt increase can be attributed to the capture of some component of the exhaust products which does not remain on the crystal at 172°K . The capture of yet another species is indicated by the increase to 10^{-3} gm/sec/sr of deposited mass at 106°K .

By using the analytical exhaust plume expansion correlation referred to earlier, it is possible to calculate the total mass flux per unit solid angle at the plume centerline. If the measured amount of centerline contamination is divided by the expected total centerline mass flux, the percent of the total centerline mass flux which is deposited on the crystals can be approximated. This percentage is shown in Figure 15 for the baseline duty cycle at crystal temperatures of 106°K , 144°K , and 172°K .

An assay of the propellant, prior to the addition of distilled water for runs 13 and 14, revealed that it contained 0.71% water and 0.55% aniline by mass. Moynihan has detected various amounts of methane in monopropellant thruster exhaust gas samples (Refs. 16,17). This methane most likely results from the breakdown of the aniline within the thruster catalyst bed. Since methane has a normal boiling point of 111.5°K (Ref. 26), it is unlikely that it contributes to the contamination shown in Figure 15.

In tests involving a Hamilton Standard REA 10-12 engine of nominally 0.44N (0.1 lbf) thrust, Moynihan (Ref. 16) has also demonstrated that the amount of water detected in the exhaust gas sample agrees well with the amount of water in the propellant assay, thus suggesting that the water survives its passages through the catalyst bed.

Prior to loaning the REA 10-18 thruster to AFRPL for the present experiment, Hamilton Standard obtained an exhaust gas sample while firing the engine in a 60 second steady state run. The sample was taken at an inlet pressure of 1344 kPa (195 psia) with an unknown propellant composition. The sample was delivered to JPL with the thruster and was subsequently analyzed manometrically and with a mass spectrometer. Hydrazine was detected using a colorimetric analysis. No attempt was made to determine the amount of water or hydrocarbon in the gas sample. The result of this analysis is given in Table VI, where water and aniline have been shown in the same proportion as determined from the assay of the propellant used in the present contamination experiment. Also shown in Table VI are the condensation temperatures of each of the constituents for a nominal MOLSINK operating pressure of 10^{-4} Pa (7.5×10^{-7} torr).

Moynihan detected as much as 1.6% by mass of unreacted hydrazine at a pulse-width of 1 second; it is thus reasonable to expect that a greater amount of unreacted hydrazine will appear in the exhaust plume at a duty cycle of 100 ms on and 10 seconds off than was evident during the steady state run for which the sample of Table VI is characteristic.

By comparing the relative orders of magnitude of the contaminants shown in Figure 15 with the results from Table VI, it may be inferred that the preponderance of deposited mass at 106°K is ammonia, while the bulk of the contaminant at 144°K is probably water and some hydrazine. While the aniline might be

expected to show up at a crystal temperature of 172°K, it clearly does not show up in proportion to its availability in the propellant, thus providing an additional argument for its decomposition within the catalyst bed.

TABLE VI. Gas Sample Constituents and Capture Temperature

Constituent	Mass in Sample (Grams)	Mass (%)	Condensation Temperature at 10^{-4} Pa MOLSINK Pressure ^(a)
H ₂	2.8×10^{-2}	8.1	4°K
N ₂	2.3×10^{-1}	66.5	26°K
NH ₃	8.37×10^{-2}	24.2	101°K
H ₂ O (b)	---	0.71	159°K
N ₂ H ₄	40×10^{-6}	0.012	165°K (Ref. 15)
Aniline (b)	---	0.55	190°K

Percent Ammonia Dissociation (c) = 65.5%

(a) Extrapolated from the data of Reference 26 except as shown.

(b) Assumed to be the same as found in the propellant.

(c) Calculated using the mole fraction ratio of H₂/NH₃ to account for any dissolved N₂ pressurant in the propellant.

Tests 13 and 14 were conducted using the baseline duty cycle and propellant with 1.8% water. The results, for crystal temperatures of 144°K and 172°K, are shown in Figure 16. The data for the baseline runs 2, 3, and 11 are also shown for comparison.

The propellant with 1.8% water produces a uniform increase in the measured contamination over that of the propellant with 0.71% water. This increase is evident at all QCM locations where data is available for comparison, and is obvious at both crystal temperatures of 144°K and 172°K, even despite the data scatter at 172°K.

The plume asymmetry of run 11 is especially obvious in Figure 16. This is particularly unfortunate since one would like to compare runs 11 and 13 as they were both conducted at about the same state of thruster life (see Table III). By assuming 1) that the same proportion of the water in the propellant remains on the crystals for both the 0.71% and 1.8% cases, and 2) that the remaining contaminants are unaffected by the water addition, a calculation of the percent contamination due to the water in the propellant may be made for each crystal. For run 11, the results indicate 14-48% water contamination at a crystal temperature of 144°K. The large variation is directly attributable to the skewness of the run 11 plume, and it is felt that the combined effects of skewness and thruster life render these figures ambiguous at best. A similar analysis was performed for the runs conducted at a crystal temperature of 172°K. Values of 26-70% water were obtained for the contamination produced by propellant with 0.71% water, and the data scatter is so great that little confidence can be given these figures either. It is important to recognize, however, that the water does in fact show up as a contamination on a 172°K surface, even though it may subsequently vaporize if exposure to a simulated space environment is continued.

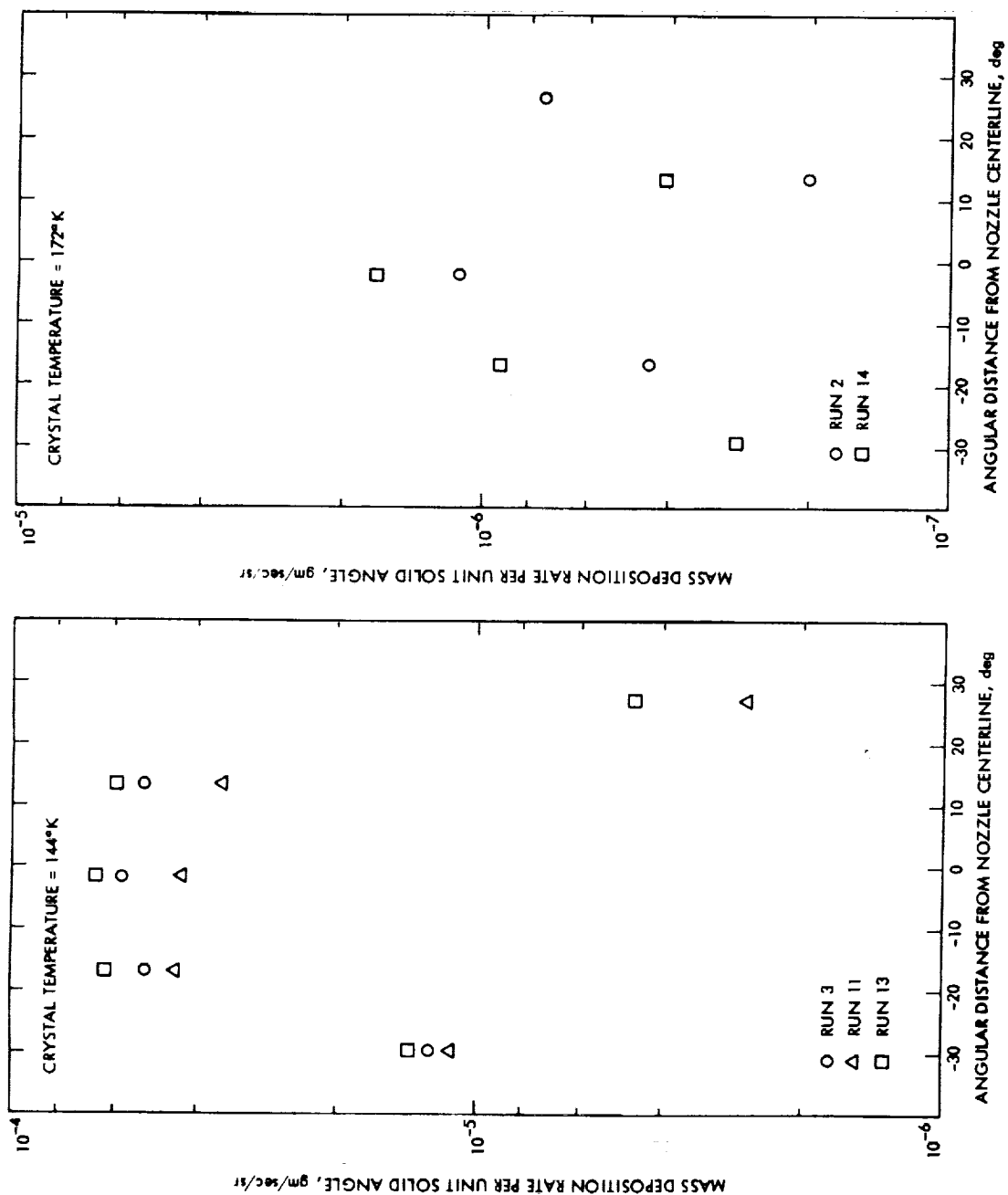


Figure 16. Effect of Water Addition to Propellant

Esenwein (Ref. 21) reports a variation of from 1 to 100 $\mu\text{gm}/\text{cm}^2$ in the amount of hydrazine or hydrazine compounds remaining on different surfaces at ambient temperatures after prolonged exposure to a simulated space environment; he offers hydrazine hydrate, $\text{H}_2\text{NNH}_2\text{H}_2\text{O}$, as a candidate residue. Chirivella (Ref. 25) has also reported traces of contaminants remaining on QCM crystal surfaces at room temperature after monopropellant thruster testing similar to that conducted for this study. Brill (Ref. 19) has witnessed snow-white deposits, believed to be raw hydrazine, on a surface exposed to a hydrazine thruster plume. These deposits subsequently vaporized leaving a slight film on the sample. The relatively miniscule amount of contaminant shown in Figure 15 at crystal temperatures of 172°K and above is thus most likely to consist of: 1) small amounts of water and hydrazine, the bulk of which probably revaporize after removal of the incident flux; 2) hydrazine compounds, which will remain on the surface up to room temperature; 3) any undecomposed aniline; and 4) other impurities which may have been in the propellant, including trace metals and particulates.

The tests conducted at crystal temperatures of 228°K and 256°K detected no mass accretion for run lengths of several thousand seconds duration. In previous MOLSINK testing with another thruster, Chirivella (Ref. 25) also detected no contaminants at a QCM temperature of 255°K, but some small mass accretion was evident during runs of several hours duration at a crystal temperature of 233°K.

C. Duty Cycle Effects

Three different duty cycles were run during the testing. These included pulse widths of 25, 100, and 200 milliseconds and off-times of 5, 10, and 20 seconds, respectively. The results for these three duty cycles are plotted in Figure 17 at crystal temperatures of 144°K and 172°K. The plume asymmetry is again evident at 144°K for the 100 ms/10 sec and the 25 ms/5 sec runs without the thruster heat shield, but is less obvious at 100 ms/10 sec with heat shield and 200 ms/20 seconds without. This demonstrates the non-repeatability of the skewness. Data scatter at a crystal temperature of 172°K is again pronounced, with the centerline QCM J again yielding the most reliable values of mass deposition rate.

The data from QCM J are shown in Figure 18 as a function of the average propellant mass flowrate to the thruster. The flowrate for run 11 and 12 was assumed to be the same as for run 14, since 14 is close to 11 and 12 in terms of thruster life, and because the addition of the small amount of water for run 14 does not affect the propellant density appreciably. The volumetric flowrate from the piston flowmeter was converted to a mass flowrate using a density of 1 gm/cm³ for the propellant, which is consistent with the measured propellant inlet temperature of 297-300°K (75-80°F) for all runs. The increase in the centerline mass deposition rate with propellant flowrate at a crystal temperature of 144°K appears to be entirely due to the increase in the water flowrate. The dashed line indicates a 30% increase in deposition rate corresponding to the 30% variation in propellant flowrate; the data follow the same trend. An increase in the deposition rate with propellant flowrate is also evident at a crystal temperature of 172°K, although in a much less interpretable manner.

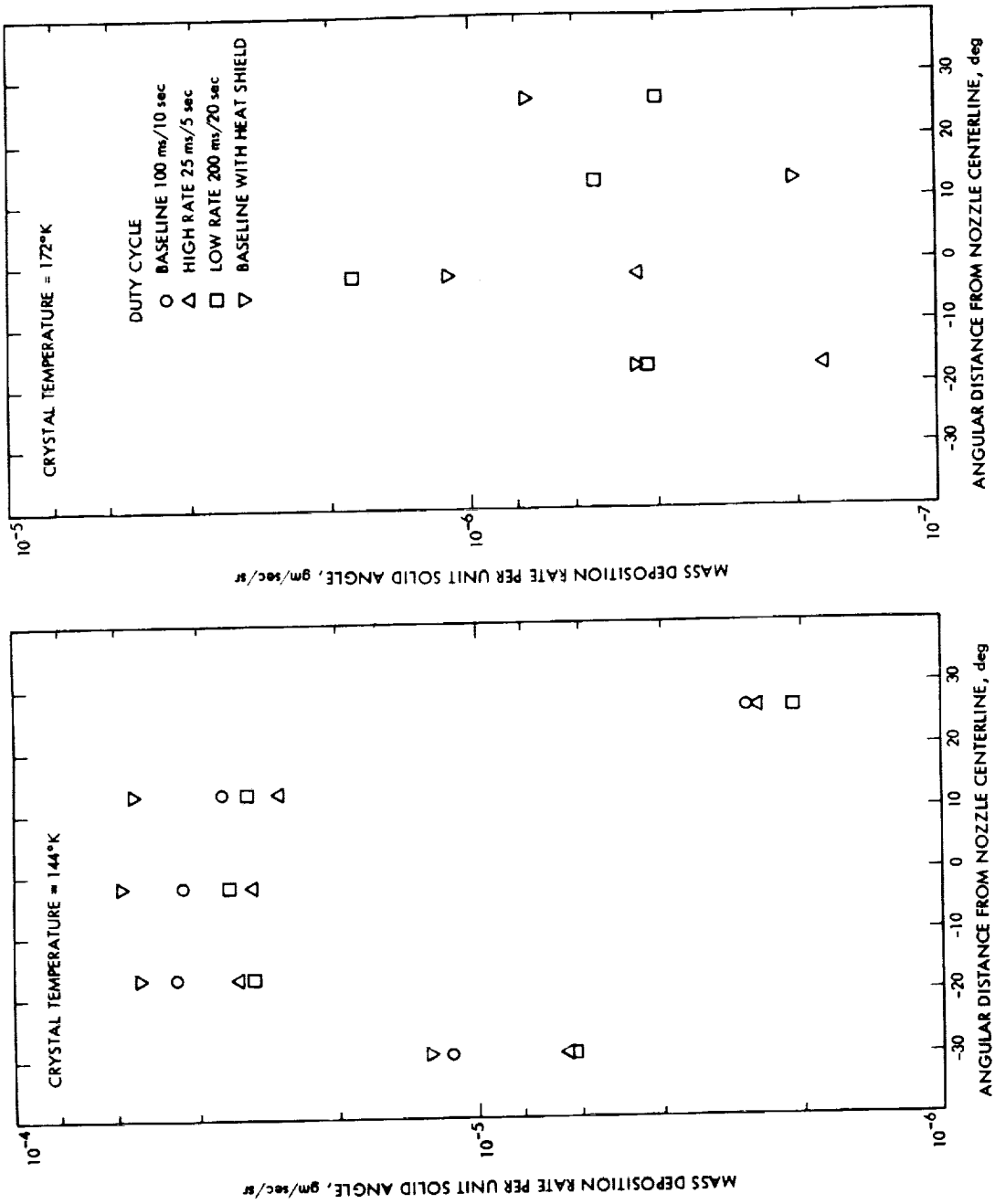


Figure 17. Effects of Duty Cycle

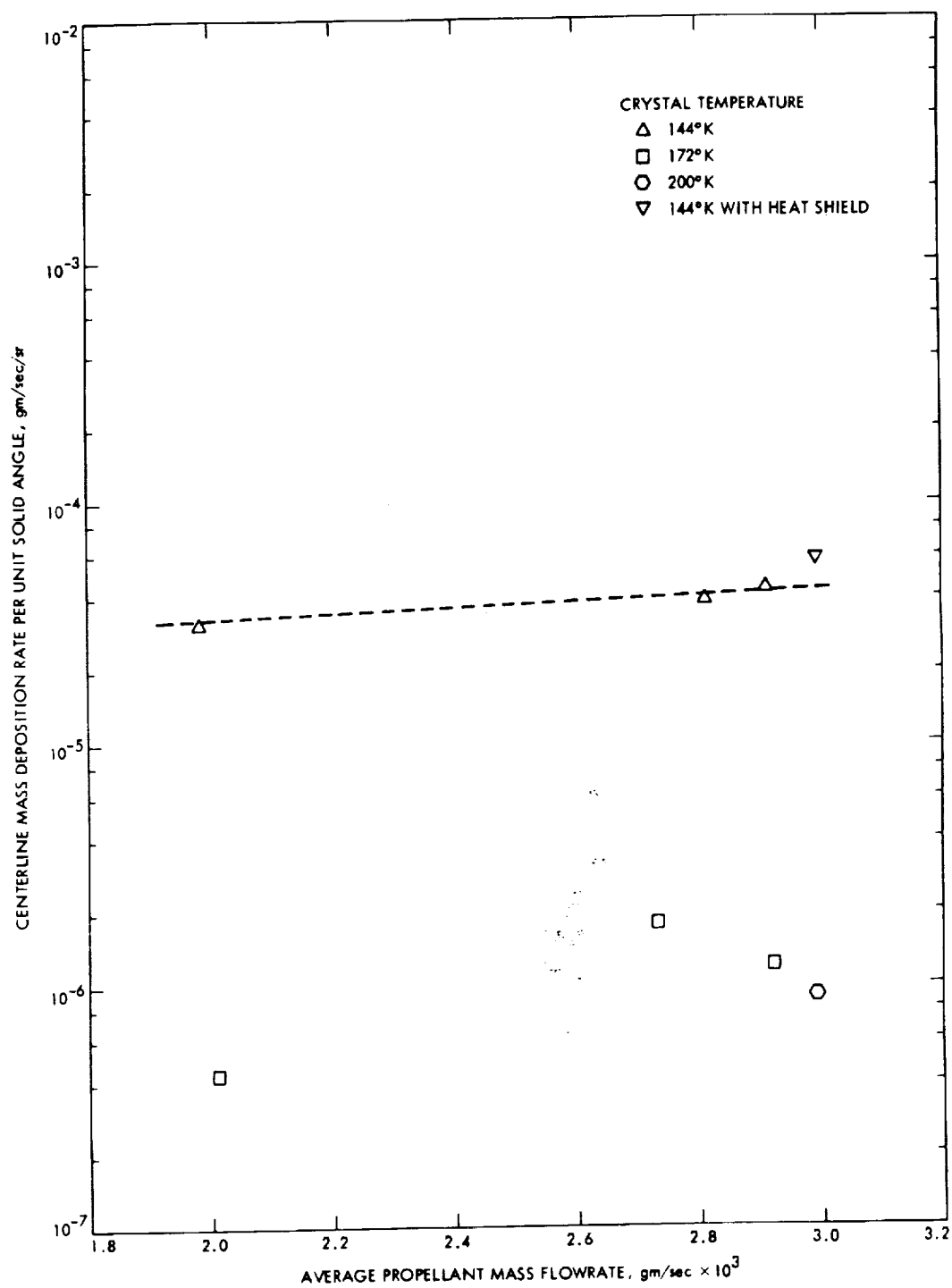


Figure 18, Centerline Deposition Versus Propellant Flowrate

By dividing the measured centerline deposition rate by the calculated centerline mass flux, the effects of flowrate can be removed. Figure 19 is a plot of the normalized centerline mass deposition rate versus the commanded valve on-time. At a crystal temperature of 144°K , a 12% decrease occurs in the measured normalized mass deposition rate, for the thruster without heat shield, as the thruster valve on-time is increased from 25 to 200 milliseconds. This is exactly what one would expect if any undecomposed hydrazine was appearing in the plume. At 172°K , on the other hand, it appears that a 210% increase in deposition is experienced as the pulse width increases from 25 to 200 milliseconds. One interpretation which can be given this behavior is that the desorption from the crystal surface at a given temperature will occur at the same rate for all three pulse widths while the incident mass flux should increase in proportion to the valve on-time. Since the deposition of either water or hydrazine at a crystal temperature of 172°K would be dependent upon a localized pressure due to the incident molecules, any increase in the length of time during which this pressure is extant would increase the measured deposition. The occurrence of mass desorption from the QCMs at a crystal temperature of 172°K after thruster shutdown seems to verify this mechanism of mass accretion.

The total data excursion at each crystal temperature is noted as a percent of the total calculated centerline mass flux in Figure 19. Clearly, if even one of the three data points upon which the deposition rate trends have been based is in error the results would be inconclusive. However, even if the suppositions discussed above relating to Figure 19 are not specious, the effects of pulse width do not appear to be significant in terms of potential contamination produced by the thruster, except as the duty cycle affects the average propellant flowrate.

D. Thruster Life Effects

The mass deposition rates for the baseline duty cycle at crystal temperatures of 144°K , 172°K , and 200°K are shown in Figures 20 and 21 for each QCM location. The contamination recorded at a crystal temperature of 144°K decreases as the thruster is aged, while the deposition rates at 172°K and 200°K increase. In fact, the after-aging baseline tests at 172°K and 200°K yielded the most consistent and easily interpretable QCM frequency-time plots of any runs at these crystal temperatures. An examination of the 200°K data taken after aging reveals a uniform plume profile detected at all QCM locations, as opposed to the great scatter evidenced during pre-aging testing.

A summary of the effects of thruster life on the propellant flowrate, equilibrium catalyst bed temperature, and the normalized centerline mass deposition rates is given in Figure 22. (Lines have been drawn through the data of Figure 22 for clarity only and are not meant to imply a functional relationship.)

The decrease in propellant flowrate with increasing number of pulses is not an uncommon phenomenon in monopropellant thruster testing. It is attributed to an increase in pressure drop across the catalyst bed due to tighter packing of the catalyst particles. The number of catalyst fines generated increases with the number of starts, and these fines tend to plug the interstices between catalyst particles before eventually working their way out of the nozzle. In addition,

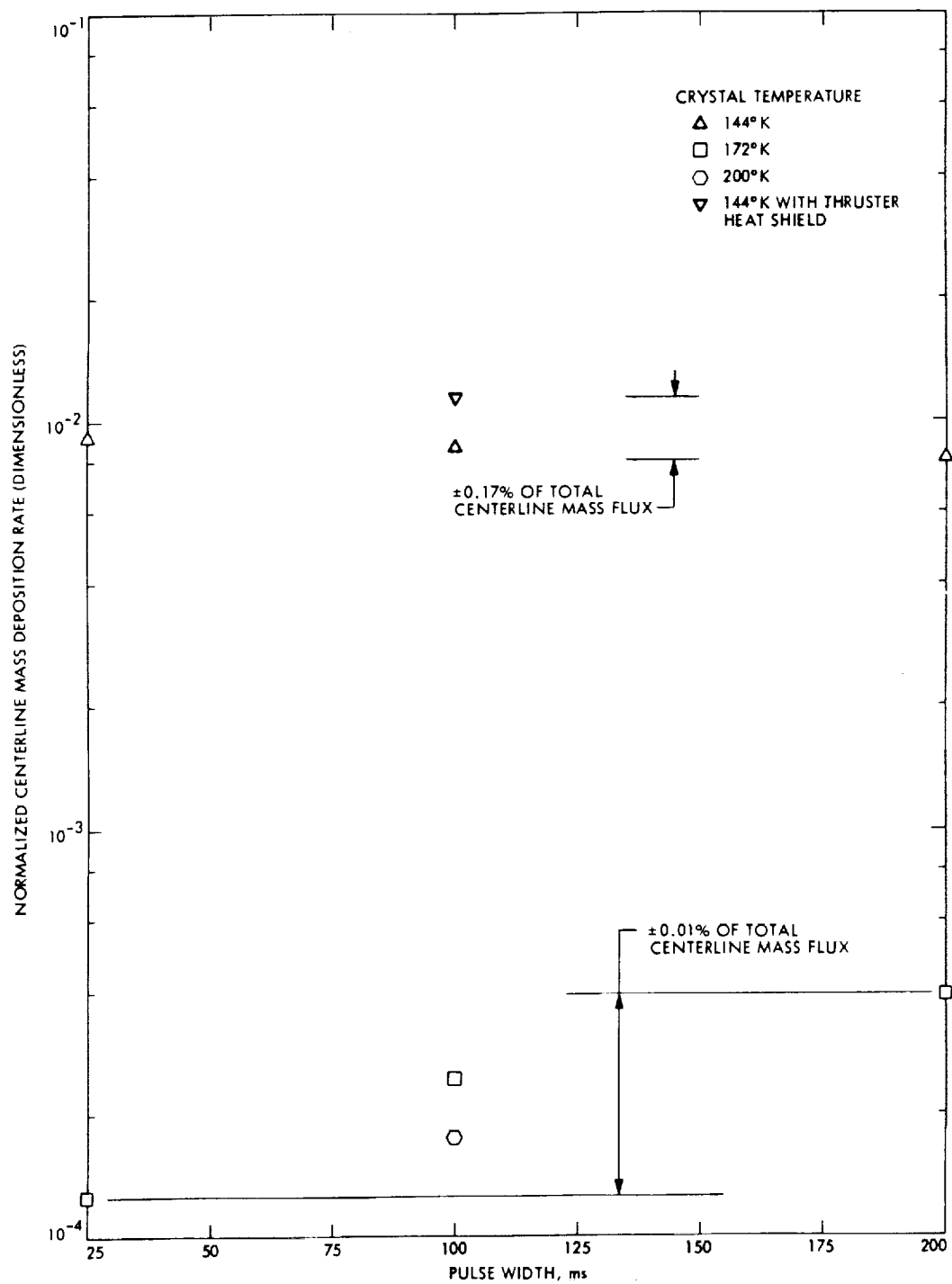


Figure 19. Effect of Pulse Width

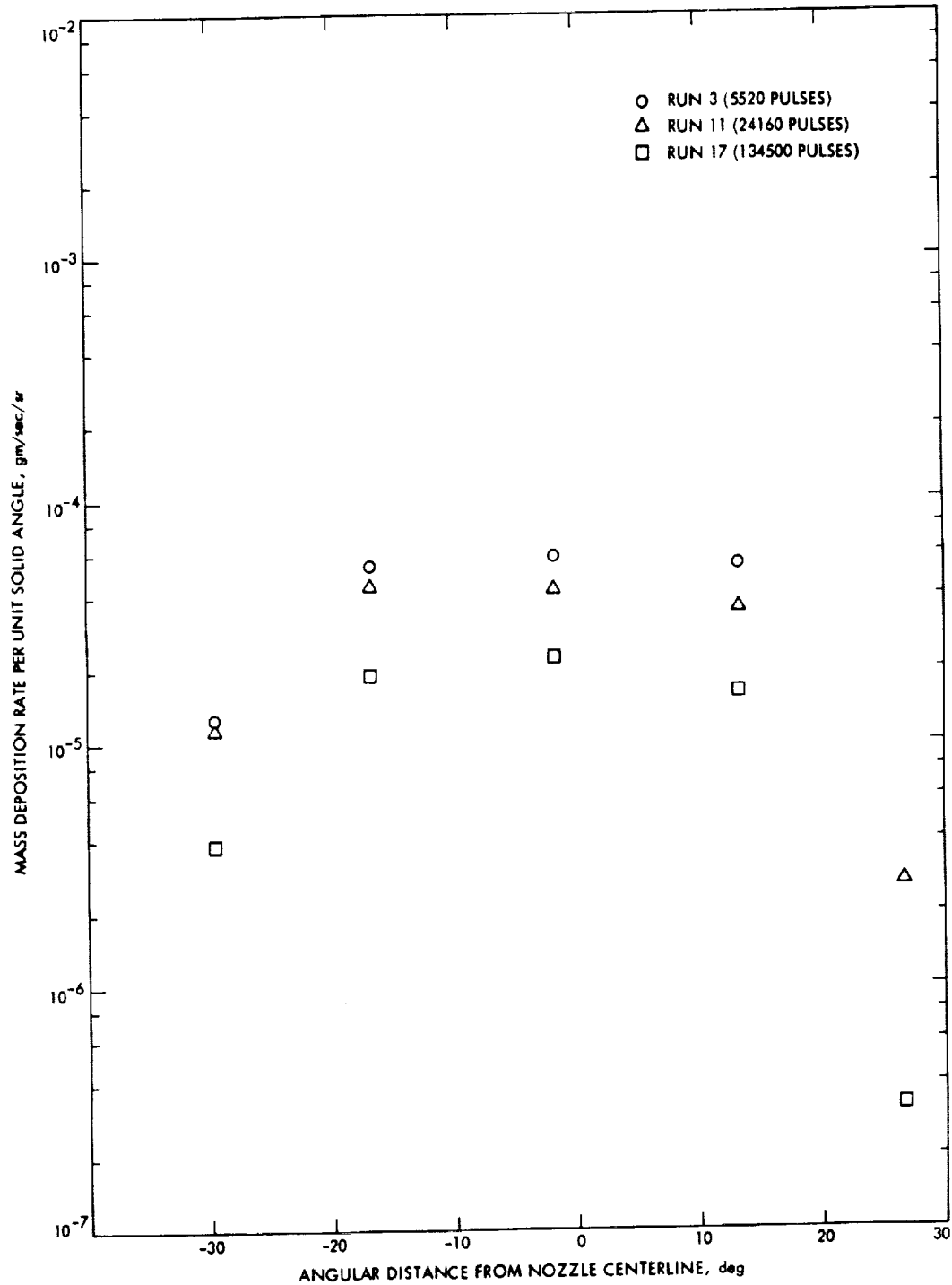


Figure 20. Effects of Thruster Life at a Crystal Temperature of 144°K

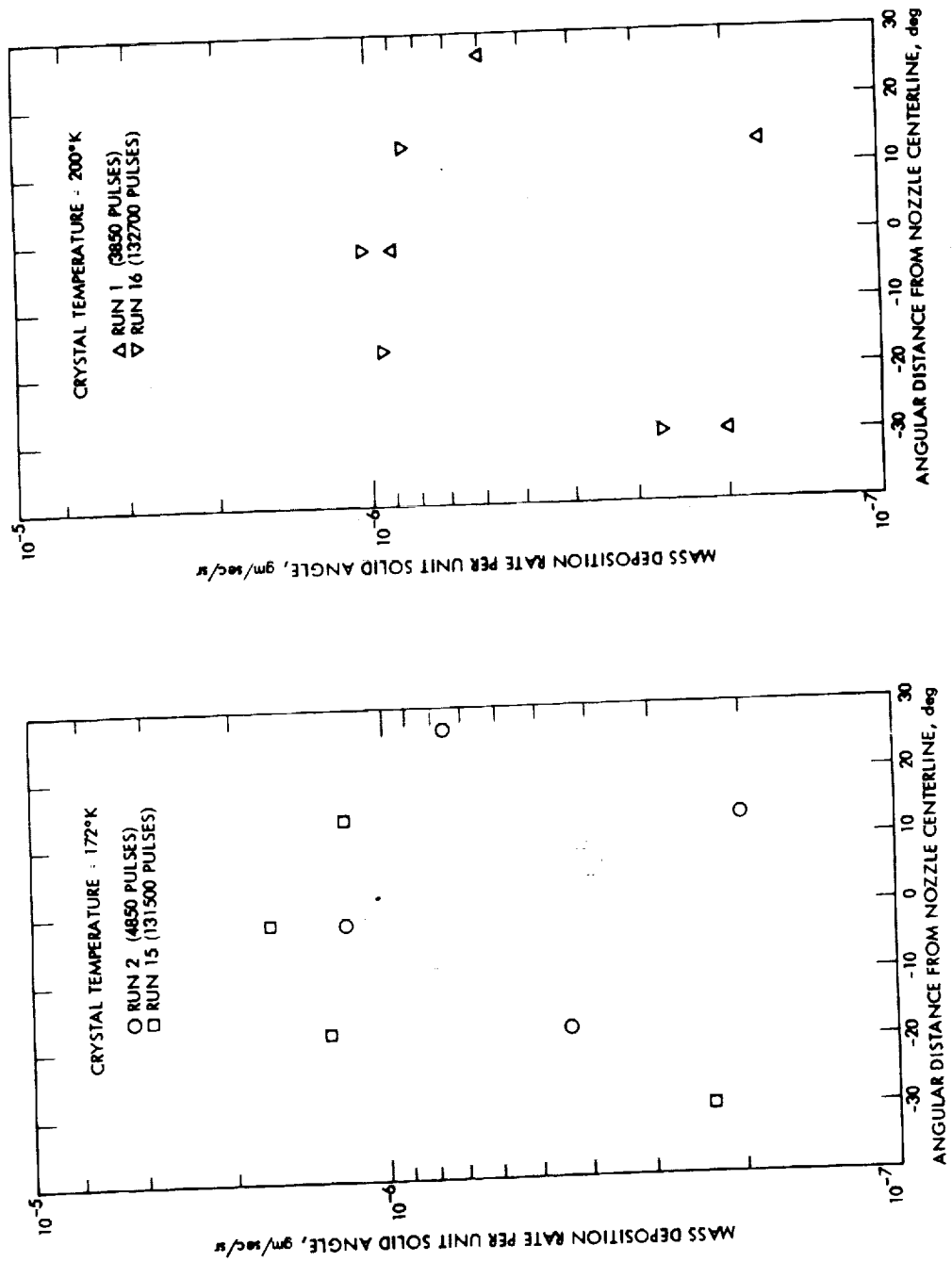


Figure 21. Effects of Thruster Life at Crystal Temperatures of 172°K and 200°K

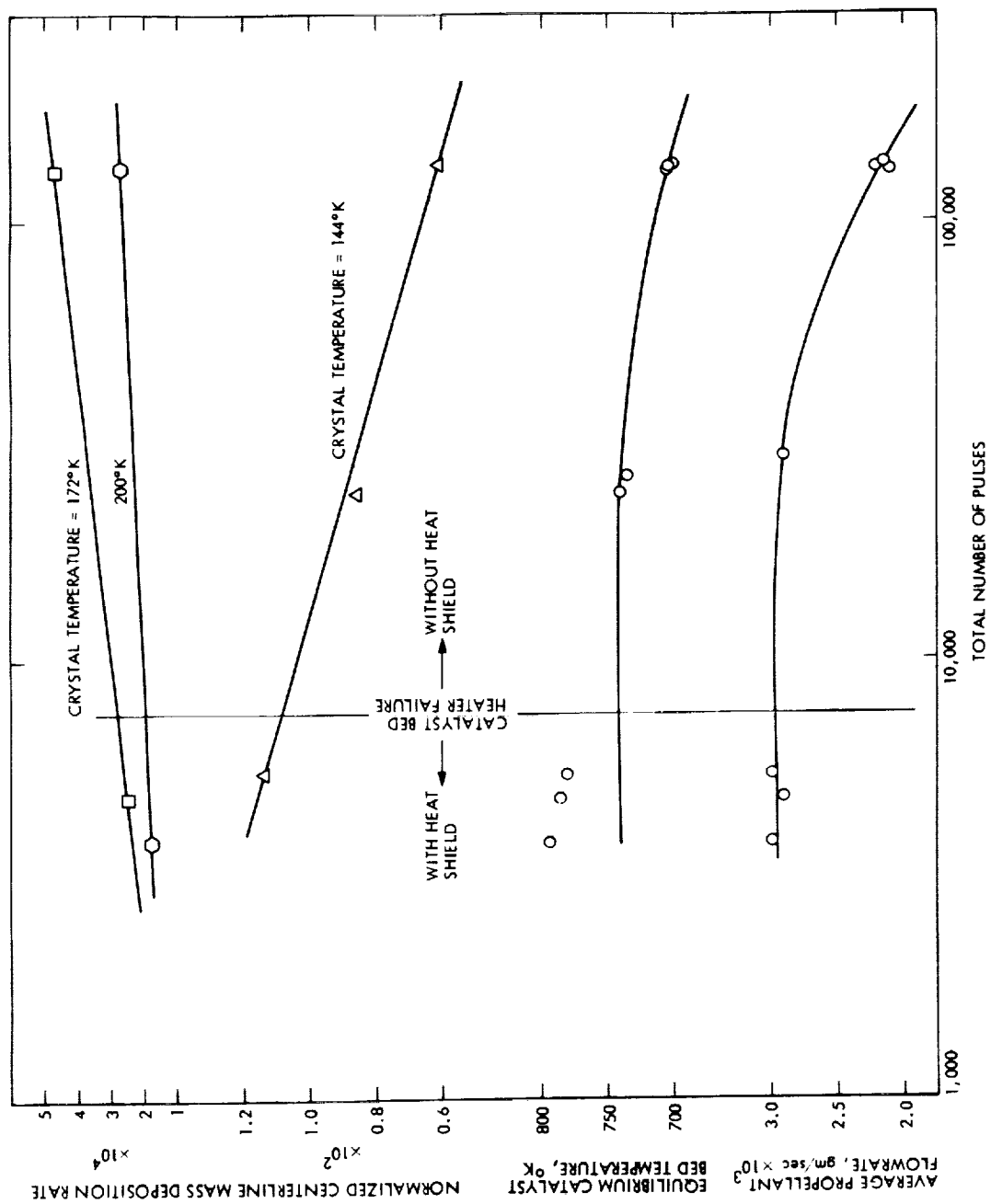


Figure 22. Effects of Thruster Life

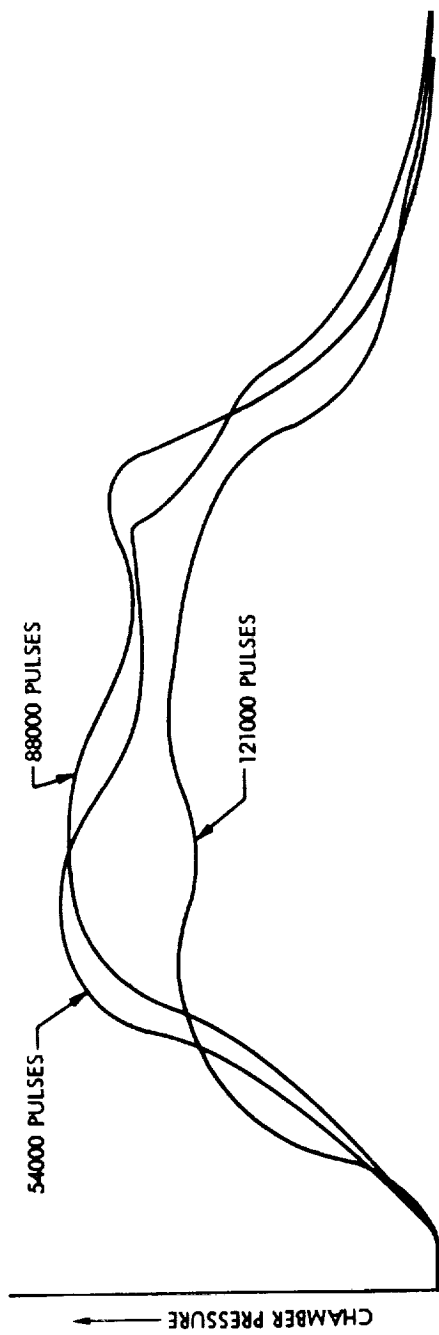
the hot firing of the thruster results in a shrinkage of the catalyst material, thus further decreasing the total catalyst bed volume. During testing with an experimental 4.5N thruster using 20-30 mesh Shell 405 catalyst, Sayer (Ref. 8) has noted a 36% decrease in the catalyst pack volume after 500 ambient temperature starts. Catalyst weight loss accounted for 29% of the decrease while the 7% difference was attributed to catalyst material shrinkage. A 49% propellant flowrate decrease and a 1300% increase in pressure drop across the catalyst bed were also observed. These results, although greatly dependent upon catalyst retention techniques and injector design, give some insight into the results shown in Figure 22. Figure 23 depicts the change in the chamber pressure pulse shape during the aging sequence. These traces were obtained from an oscilloscope during firings with a 90 ms pulse width. A 30% decrease in peak chamber pressure with age is evident, even though the thruster was not subjected to ambient temperature starts.

After the 100,000 pulse aging sequence, the number of pulses which could be run before the MOLSINK chamber avalanched (see Section II-A) continually decreased with time. This would indicate that more hydrogen was being injected into the MOLSINK than during pre-aging testing, which would in turn imply an increase in the percent ammonia dissociation. The increase in the percent ammonia dissociation can be attributed to the longer residence time of the gases within the catalyst bed due to an increase in the resistance to flow through the bed. The decrease in the equilibrium catalyst bed temperature shown in Figure 22 is consistent with the supposition of increased ammonia dissociation since this reaction is endothermic.

The decrease of 46% in the contaminants measured at a crystal temperature of 144°K can also be attributed to an increase in the gas residence time within the catalyst bed, coupled with the availability of more active catalyst sites per molecule due to the reduced propellant flowrate. It has previously been established that any undecomposed hydrazine appearing in the plume will show up as contamination at the 144°K surface temperature, and increased hydrazine decomposition could account for the decreased deposition shown in Figure 22.

The most perplexing results are found at the higher crystal temperatures. At 172°K a 92% increase in contamination is observed, while a 55% increase is seen at 200°K. This might be the result of undecomposed aniline leaving the thruster, although this would seem to be at odds with the conclusion drawn about increased hydrazine and ammonia decomposition.

The postulated decrease in raw hydrazine detected at 144°K would also argue against the formation of greater amount of hydrazine hydrate or other hydrazine compounds on the 172°K and 200°K crystal surfaces since less hydrazine would be available for this formation. It is possible that the carbon buildup within the catalyst bed from the aniline decomposition reaches such a level that hydrocarbon formation and expulsion become likely. Without any additional data, however, the origin and identification of the contaminants deposited at crystal temperatures of 172°K and 200°K will remain unknown.



48

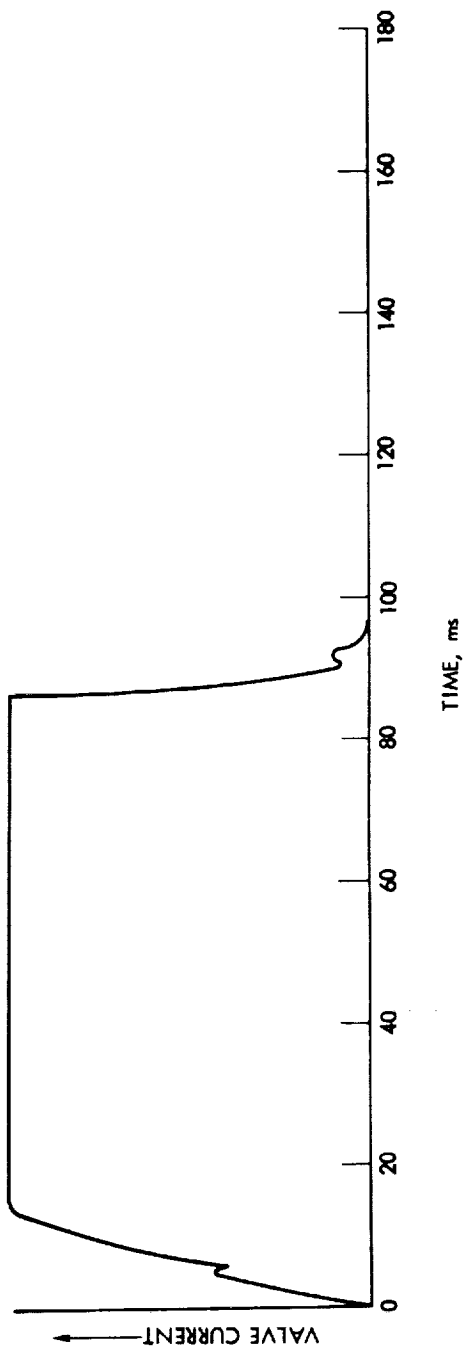


Figure 23. Thruster Chamber Pressure Pulse Shape During Aging Sequence (90 ms Pulse Width)

E. Effect of Pulse Train Transients

The first few pulses in a pulse train generally occur at a catalyst bed temperature which is lower than the train equilibrium temperature for a given duty cycle. These initial pulses might be expected to generate different amounts of contaminants than the later pulses in the train. Runs 8, 9, and 10 were short runs of 60 pulses each at a duty cycle of 200 ms on and 20 seconds off, and were conducted at a crystal temperature of 144°K. The digital data acquisition system sampled each of the QCMs every 88 seconds, or after approximately every fourth pulse, yielding 14 data points. These data points were then fitted in a least squares sense with cubic splines having continuous second derivatives. The derivatives of the resulting spline fits were then converted to mass deposition rates as discussed in Appendix A. Run 7 was conducted under the same conditions as runs 8, 9, and 10, except that it was extended for 419 pulses; in this case the data from the first 60 pulses were fit with one spline while the remaining data were fit with another. The mass deposition rate in gm/cm²/sec from the centerline QCM J for each of the four runs is plotted as a function of pulse number in Figure 24. The deposition rates were obtained from the fitted data at five-pulse intervals. While the numerical procedures used to fit the data will clearly have some influence on the results (note especially run 8), it is obvious from Figure 24 that a decrease in mass deposition rate is evident as the number of pulses increase for all four runs. The initial mass deposition rates shown are 19-42% higher than the equilibrium mass deposition rate obtained from run 7.

Thermal equilibrium in the catalyst bed is achieved for the 200 ms on/20 sec off duty cycle after approximately 30 pulses without the thruster heat shield; a duty cycle of 100 ms on/10 sec off requires 60 pulses, and a duty cycle of 25 ms on/5 sec off requires approximately 150 pulses to obtain the train equilibrium conditions. If the increased deposition is due to undecomposed hydrazine being expelled during the thruster warmup period, one would expect that the shorter pulse widths would produce even greater amounts since the temperature achieved per pulse is less.

V. CONCLUSIONS AND RECOMMENDATIONS

Based upon the results presented in the previous section, the following conclusions are drawn:

- (1) The spread of the monopropellant thruster exhaust contaminants which adhere to a 144°K surface can be approximated to good accuracy by the Hill and Draper (Ref. 31) correlation for regions of the plume within 30° of the nozzle centerline if a proper selection of the ratio of specific heats, γ , is made. For the present experiment a value of $\gamma = 1.41$ was indicated, which is equivalent to an evaluation of γ at a temperature near that of the nozzle exit. The exhaust plume profile of a small monopropellant thruster might be calculated within this region using these results if it is assumed that the other constituents of the exhaust expand at a comparable rate.
- (2) Testing in the MOLSINK facility at a nominal pressure of 10^{-4} Pa (7.5×10^{-7} torr) revealed that ammonia from a monopropellant thruster exhaust is the predominant contaminant on a surface at a temperature of 106°K. Water will be a contaminant on surfaces at 144°K in quantities directly proportional to its availability in the propellant.

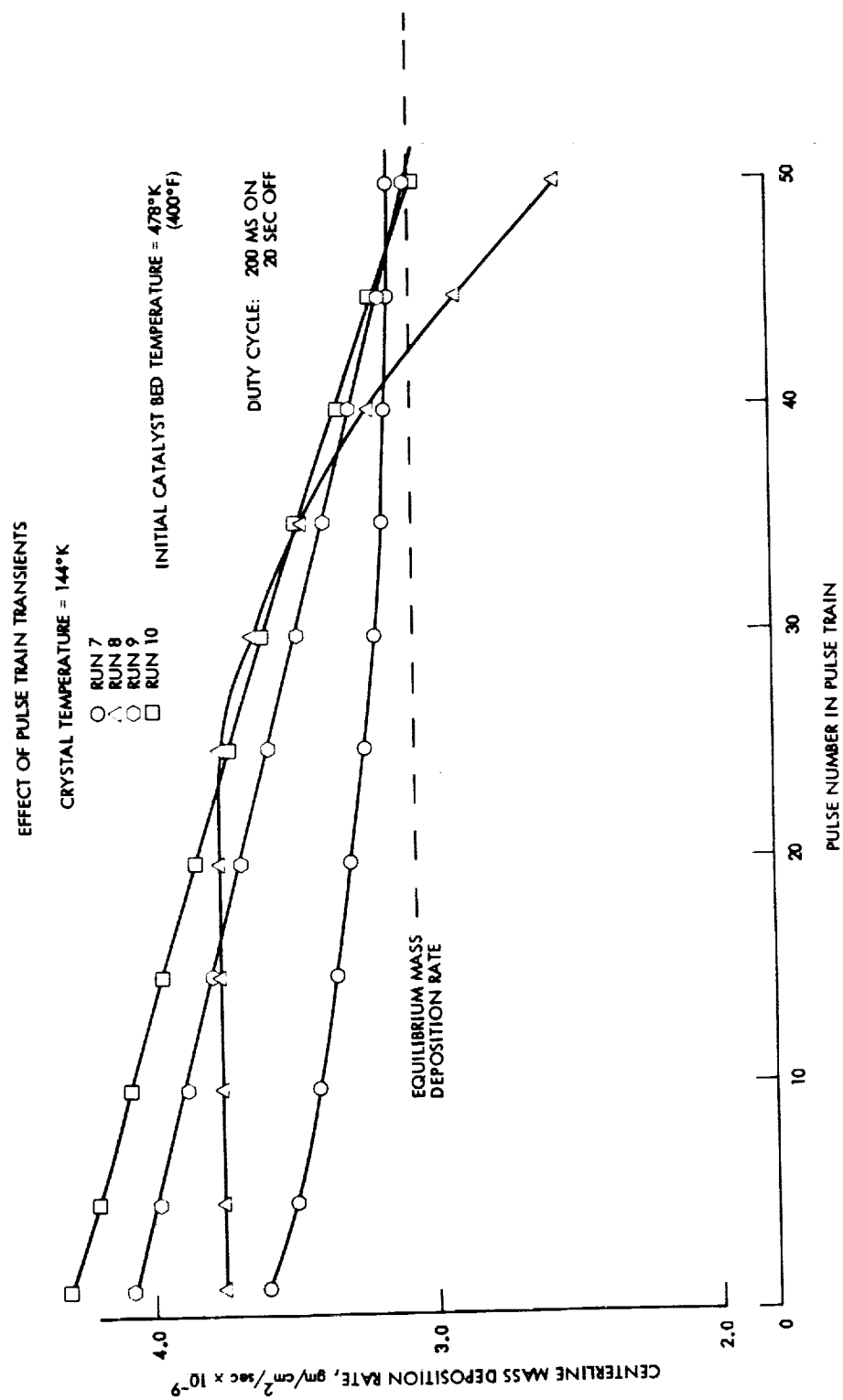


Figure 24. Effect of Pulse Train Transients

Undecomposed hydrazine will also probably remain on surfaces of around 144°K. Hydrazine and water may also show up on surfaces of 172°K and 200°K, but subsequent desorption is likely if exposure to a space environment is maintained. Less than 0.05% of the incident mass flux will remain on surfaces above 172°K for any appreciable length of time.

- (3) For the three duty cycles tested, 25 ms on/5 sec off, 100 ms on/10 sec off, 200 ms on/20 sec off, no significant change was noted as a function of duty cycle in the measured deposition rates on surfaces at 144°K or 172°K, except as the duty cycle affected the average propellant flowrate during the pulse train.
- (4) For the monopropellant thruster used in this experiment, aging of over 130,000 pulses seemed to produce less ammonia and a 46% decrease in the mass deposition which was measured at a surface temperature of 144°K, the latter possibly corresponding to a decrease of undecomposed hydrazine in the plume. An increase in the contaminants which were deposited at surface temperatures of 172°K and 200°K was also noted, but insufficient data were available for identification.
- (5) Up to 42% higher mass deposition rates were seen at a surface temperature of 144°K for the first pulses in a train at a duty cycle of 200 ms on/20 sec off with a 478°K (400°F) initial catalyst bed temperature.

Based upon the experience gained in the course of this experiment, the following recommendations are offered:

- (1) The use of the MOLSINK facility to obtain contamination data from monopropellant thrusters was a natural continuation of previous efforts to define the thruster exhaust plume flow field. However, the use of the QCM for contamination studies should be combined with additional diagnostic tools so that the QCM data is more easily interpretable, especially as relates to contaminant species.
- (2) Measurements of the monopropellant thruster contamination on surfaces at 172°K and 200°K were much less successful than at lower temperatures due to the small mass accretion rates experienced at the higher temperatures. Since this is a critical temperature band for many spacecraft components, additional measurements of the mass deposition rates and identification of the contaminant species of these temperatures is warranted. At these low deposition rates, a more sensitive QCM, perhaps with a 10 MHz crystal, should be utilized.
- (3) The QCMs should be calibrated against some secondary standard, preferably in situ, over the entire temperature range of operation. An investigation of molecular scattering after passing the collimator and molecular migration towards the doublet reference electrode should be undertaken, especially as pertains to non-normal angle of incidence.

REFERENCES

1. Martinikovic, P.J., "Monopropellant Exhaust Contamination Investigation," AFRPL-TR-69-72, Air Force Rocket Propulsion Laboratory, Edwards Air Force Base, CA, April 1969.
2. Dunn, B.D., and Steinz, J.A., "Contamination and Heating Effects of a Hydrazine Thruster Intended For Use On Board the Scientific Geostationary Satellite," ESRO-TM-157 (ESTEC), European Space Research and Technology Centre, Noordwijk, The Netherlands, April 1974.
3. Chirivella, J.E., and Moynihan, P.I., "Hydrazine Rocket Plume Deposits Measured With Quartz Crystal Microbalances," Proceedings of the 7th JANNAF Plume Technology Conference, Redstone Arsenal, Huntsville, AL, April 1973.
4. Davis, L.P., and Witbracht, I.L., "Thruster Contamination Prediction For NATO III Satellite," AFRPL-TR-75-67, Air Force Rocket Propulsion Laboratory, Edwards Air Force Base, CA, December 1975.
5. Rogers, J.F., "Data From a Synchronous Altitude Satellite Quartz Crystal Microbalance Monitor," Eighth Conference on Space Simulation, NASA SP-379, Silver Spring, MD, November 1975.
6. Russi, M.J., "A Survey of Monopropellant Hydrazine Thruster Technology," Paper 73-1263, AIAA/SAE 9th Propulsion Conference, Las Vegas, NV, November 1973.
7. Marteney, P.J., and Kesten, A.S., "Catalyst Particle Wetting and Breakup in Hydrazine Systems," Journal of Spacecraft and Rockets, Vol. 13, No. 7, July 1976, pp. 430-434.
8. Sayer, C.F., and Southern, G.R., "The Comparative Testing of the Shell 405, CNESRO-1, and RPE 72/1 Hydrazine Decomposition Catalysts," Paper 73-1266, AIAA/SAE 9th Propulsion Conference, Las Vegas, NV, November 1973.
9. Quirk, J.A., "Life Evaluation of Monopropellant Hydrazine Thrusters," 1972 JANNAF Propulsion Meeting, November 1972.
10. Moseley, V.A., et al., "Long Life Monopropellant Design Criteria (5 lbf Thrust Size)," AFRPL-TR-75-45, Air Force Rocket Propulsion Laboratory, Edwards Air Force Base, CA, July 1975.
11. "Advanced Development Program for Long-Life Hydrazine Engine Technology," Rocket Research Corporation, Contract F04611-76-C-0052 with Air Force Rocket Propulsion Laboratory (1976 to present).
12. Gorman, D.M., "Performance Mapping of Catalytic Hydrazine Attitude Control Thrusters," AFRPL-TR-76-81, Air Force Rocket Propulsion Laboratory, Edwards Air Force Base, CA, December 1976.

REFERENCES (Cont'd.)

13. Young, L.S., "Cooled Infrared Telescope Development," Raumfahrtforschung, Heft 6, 1976, pp. 279-285.
14. Arnold F., et al., "Infrared Spectral Reflectance of Plume Species on Cooled Low Scatter Mirrors," AFRPL-TR-73-52, Air Force Rocket Propulsion Laboratory, Edwards Air Force Base, CA, September 1973.
15. Lyon, W.C., "Thruster Exhaust Effects Upon Spacecraft," NASA TM-X-65457, Goddard Space Flight Center, Greenbelt, MD, October 1970.
16. Moynihan, P.I., and Bjorklund, R.A., "Performance Characterization Tests of Three 0.44 N (0.1 lbf) Hydrazine Catalytic Thrusters," TR 32-1584, Jet Propulsion Laboratory, Pasadena, CA, November 1972.
17. Moynihan, P.I., "Attitude Propulsion Technology for TOPS," JPL TR 32-1560, Jet Propulsion Laboratory, Pasadena,
18. Long, H.R., and Bjorklund, R.A., "Trajectory Correction Propulsion for TOPS," TR 32-1571, Jet Propulsion Laboratory, Pasadena, CA, November 1972.
19. Brill, Y.C., Stechman, R.C., and Reis, R.J., "Effects of Hydrazine Rocket Fuel on Spacecraft Materials," 14th Annual Technical Meeting, Institute of Environmental Sciences, St. Louis, MO, 1968.
20. Kruger, G.W., and Riebling, R.W., "Experimental Evaluation of Performance Losses in Monopropellant Hydrazine Reactors Using Shell 405 Catalyst," 1972 JANNAF Propulsion Meeting, CPIA Publication 228, Vol. IV, pp. 203-212, Silver Springs, MD, December 1972.
21. Esenwein, F.T., and Walker, S.C., "Effects of Hydrazine Exhaust Plumes and Propellant Spills on Selected Spacecraft Materials," Hydrazine Monopropellant Technology Symposium, CPIA Publication 160, December 1967.
22. Schuler, W.B., et al., "The Removal of Impurities From Hydrazine for Control of Contamination Caused by Rocket Engine Exhaust," AIAA Paper No. 72-1046, 1972.
23. Holcomb, L., Mattson, L., and Oshiro, R., "Effects of Aniline Impurities on Monopropellant Hydrazine Thruster Performance," Journal of Spacecraft and Rockets, Vol. 14, No. 3, March 1977, pp. 141-148.
24. Richards, R.E., and Grabb, R., "0.2 lb Monopropellant Hydrazine Thruster Test Results With MIL-Grade and Viking-Grade Propellant," AIAA Paper No. 76-657, AIAA/SAE 12th Propulsion Conference, Palo Alto, CA, July 1976.
25. Chirivella, J.E., "Hydrazine Engine Plume Contamination Mapping," ARFPL-TR-75-16, Air Force Rocket Propulsion Laboratory, Edwards Air Force Base, CA, October 1976.

REFERENCES (Cont'd)

26. Kaye, G.W.C., and Laby, T.H., Tables of Physical and Chemical Constants, Longman Group Limited, London, 1973.
27. Stephens, J.B., "Space Molecular Sink Simulator Facility Design," Journal of Spacecraft and Rockets, Vol. 3, No. 6, June 1966, pp. 844-848.
28. Stephens, J.B., "Molecular Sink," Research/Development, July 1967, pp. 42-44.
29. Van Dyke, K.D., et al., "Standards of Piezoelectric Crystals, 1949," Proceedings of the Institute of the Radio Engineers, Vol. 37, December 1949, pp. 1378-1949.
30. Bartera, R.E., "Quartz Crystal Oscillator Apparatus for Measuring Mass Accretion and Temperature Independently of Each Other," JPL Patent Case 11279, Jet Propulsion Laboratory, Pasadena, CA, April 29, 1975.
31. Hill, J.A.F., and Draper, J.S., "Analytical Approximation for the Flow from Nozzle into a Vacuum," Journal of Spacecraft and Rockets, Vol. 3, No. 10, October 1966, pp. 1552-1559.
32. Stockbridge, C.D., "Resonance Frequency versus Mass Added to Quartz Crystals," Vacuum Microbalance Techniques, Vol. 5, Plenum Press, NY, 1966, pp. 193-206.
33. Glassford, A.P.M., "An Analysis of the Accuracy of a Commercial Quartz Crystal Microbalance," AIAA Paper No. 76-438, AIAA 11th Thermophysics Conference, San Diego, CA, July 1976.
34. Heising, R.A., Quartz Crystals for Electrical Circuits, Van Nostrand, Co., NY, 1946.
35. McSkimin, H.J., Andreatch, P., and Thurston, R.N., "Elastic Modulus of Quartz versus Hydrostatic Pressure at 20° and -195.8°C," Journal of Applied Physics, Vol. 36, No. 5, May 1965, pp. 1624-1632.

APPENDIX A

Derivation of Relations Pertaining to the Quartz Crystal Microbalance

I. TEMPERATURE COMPENSATION

In Section II-B the change in crystal frequency Δf is expressed as a function of the change in deposited mass Δm and the change in crystal temperature ΔT :

$$\Delta f = C_m \Delta m + C_T \Delta T$$

where C_m and C_T are referred to as the mass and temperature coefficients, respectively. As discussed in Section II-B, for a proper selection of the crystal cut, the temperature coefficient can be reduced to an insignificant value over a limited temperature range. With proper QCM design, e.g., one employing the crystal doublet, an additional temperature compensation may be obtained as follows.

Consider two crystals, designated 1 and 2, exposed to mass deposition and temperature variation. The corresponding change in frequency can be expressed as:

$$\Delta f_1 = C_{m1} \Delta m_1 + C_{T1} \Delta T_1 \quad (A1)$$

$$\Delta f_2 = C_{m2} \Delta m_2 + C_{T2} \Delta T_2 \quad (A2)$$

If both crystals have identical piezoelectric properties and are kept at the same temperature, then

$$\begin{aligned} C_{m1} &= C_{m2} = C_m ; & C_{T1} &= C_{T2} = C_T ; & \text{and} \\ \Delta T_1 &= \Delta T_2 = \Delta T \end{aligned} \quad (A3)$$

Subtracting equation (A2) from equation (A1) and substituting the relations (A3) yields:

$$\Delta F = \Delta f_1 - \Delta f_2 = C_m (\Delta m_1 - \Delta m_2)$$

where ΔF is the beat frequency between the two crystals. If crystal 2 is protected from mass deposit such that $\Delta m_2 = 0$, then

$$\Delta F = C_m \Delta m_1 \quad (A4)$$

and the beat frequency is thus correlated with the mass deposited on the exposed crystal. In practice, the conditions $\Delta T_1 = \Delta T_2$ and $\Delta m_2 = 0$ are achieved for the doublet by screening half of the crystal with Mylar, which is transparent to the radiation environment. (See Figure 8.)

II. MASS COEFFICIENT

The following is a simplified derivation of the relationship between deposited mass and change in crystal frequency. For a more rigorous derivation which provides greater insight into the limitations of the relationships developed here, the reader is referred to the analyses of Stockbridge (Ref. 32) or Glassford (Ref. 33).

The relationship between the natural frequency f of a quartz crystal excited in the thickness shear mode and the crystal plate thickness t is given by:

$$f = N/t \quad (A5)$$

where N is a constant. The crystal thickness may be expressed as

$$t = \frac{m}{\rho A} \quad (A6)$$

where m , ρ , and A are the mass, density, and area of the crystal plate, respectively. Substituting equation (A6) into (A5) yields:

$$f = \frac{N\rho A}{m} \quad (A7)$$

By differentiating f with respect to m , an expression is obtained which relates a change in the crystal mass dm due to a change in thickness to the corresponding change in frequency df :

$$df = - \frac{N\rho A}{m^2} dm \quad (A8)$$

Solving equation (A7) for m and substituting into equation (A8) yields:

$$df = - \frac{f^2}{N\rho A} dm \quad (A9)$$

The assumption will now be made that the change in mass dm can be effected by depositing a mass other than quartz on the surface of the crystal. For finite changes, this expression becomes:

$$\Delta f = \frac{f^2}{N\rho A} \Delta m \quad (A10)$$

where f_c is the natural frequency of vibration of the crystal. (The negative sign has been dropped since it can be changed in the electronics.)

If (A10) is now compared to (A1), we get

$$C_m = \frac{f_c^2}{N\rho A} \quad (A11)$$

III. WORKING RELATIONS

The QCM beat frequency may now be expressed as

$$\Delta F = C_m \Delta m = \frac{f_c^2}{N\rho A} \Delta m = \frac{f_c^2}{N\rho} \frac{\Delta m}{A} \quad (A12)$$

The crystals employed in the present experiment were of such a thickness that $f_c = 5$ MHz. For an AT cut crystal the constant N is 1.670×10^6 Hz-mm (Ref. 34), and the density of quartz is 2.65 gm/cm³ (Ref. 35). Substituting these values into equation (A12) and rearranging yields

$$\Delta M = \frac{\Delta m}{A} = 1.77 \times 10^{-8} \Delta F$$

Dividing both sides by an incremental time Δt and letting $\Delta t \rightarrow 0$ finally yields

$$\dot{M} = 1.77 \times 10^{-8} \dot{F}$$

where \dot{M} is the mass flux per unit area, gm/cm²/sec, and \dot{F} is the time rate of change of the crystal beat frequency, Hz/sec.

APPENDIX B

Data Reduction

The beat frequency recorded at each time slice for each of the QCMs was plotted as a function of time and curvefit in the least squares sense with a twice differentiable cubic spline. This technique almost always provided a better fit to the data than a linear fit since deviations from a straight line were usually evident at the beginning and end of a test. The derivative of the fitted curve was then multiplied by a constant to convert the time rate of change of frequency to a mass deposition rate in $\text{gm/cm}^2/\text{sec}$ (see Appendix A). A frequency-time plot for QCM I during run number 2 at 172°K is shown as an example in Figure B-1. The line through the data is the cubic spline fit. The mass deposition rate obtained from Figure B-1 is shown in Figure B-2.

For each of the QCMs, a correction was made for the decrease in effective surface area due to non-normal incident flux. This consisted of dividing the mass deposition rate by the cosine of the angle of incidence on the crystal surface. The mass deposition rate per unit solid angle, gm/sec/sr , was then obtained by multiplying the corrected measured deposition rate by the square of the distance between thruster and crystal. The location of each QCM with respect to the thruster is shown in Figure 10. Not shown in Figure 10 is a displacement of 1.35 cm out of the plane of the page of the bar upon which the QCMs are mounted, and a 5° tilt of the bar away from the thruster.

The location and factors used in the reduction of the readings from each QCM are summarized below.

QCM	True Angle From Nozzle Centerline (Degrees)	Angle Between Incident Streamline and Surface Normal (Degrees)	Correction Factor	Distance From Nozzle to Crystal (cm)
H	29.72	30.16	0.865	130.47
I	16.8	17.70	0.953	118.36
J	1.89	5.95	0.995	113.37
K	13.28	14.43	0.968	116.43
L	26.80	27.34	0.888	126.94

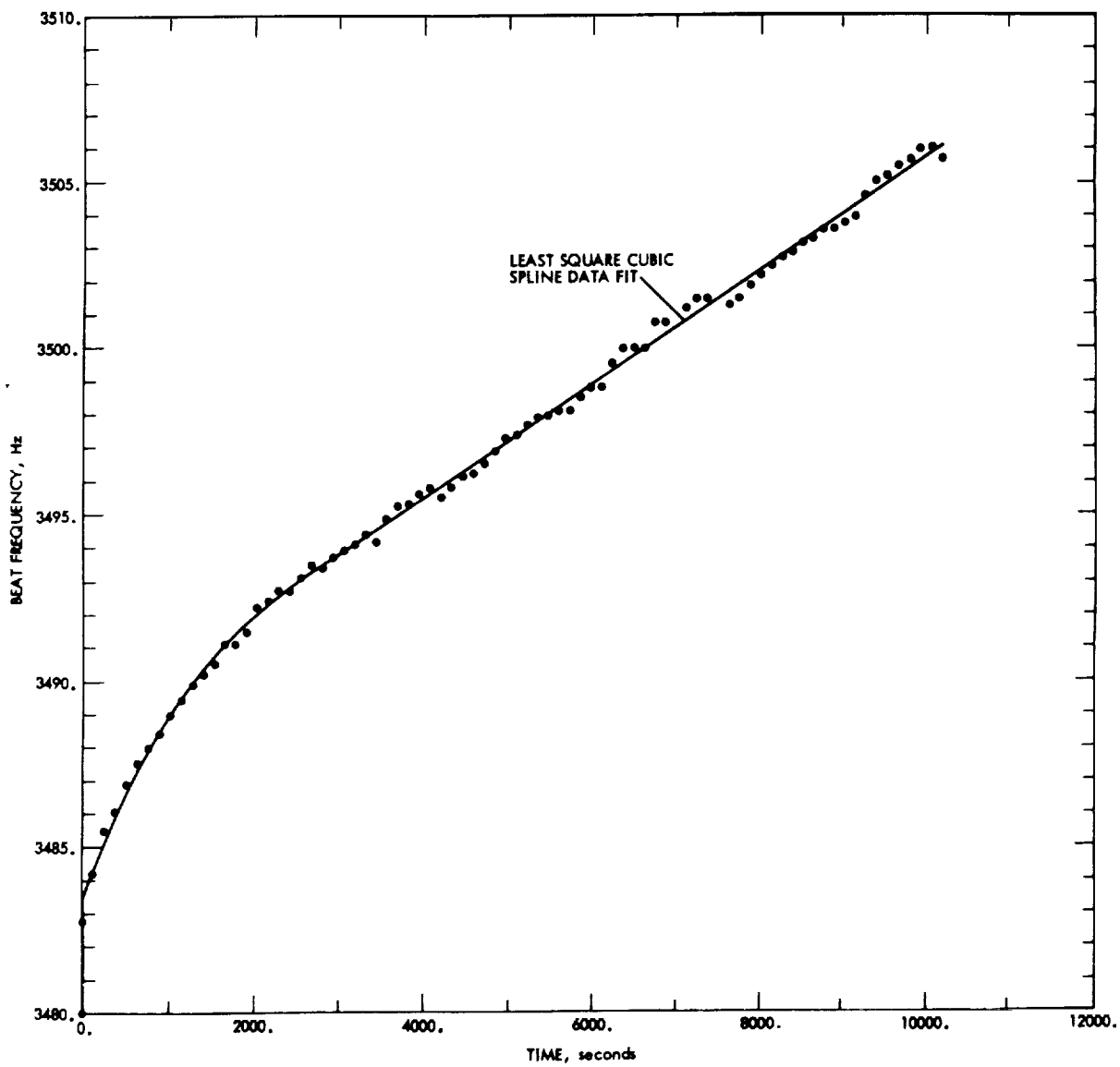


Figure B-1. Beat Frequency Versus Time
for QCM "I" During Run 2

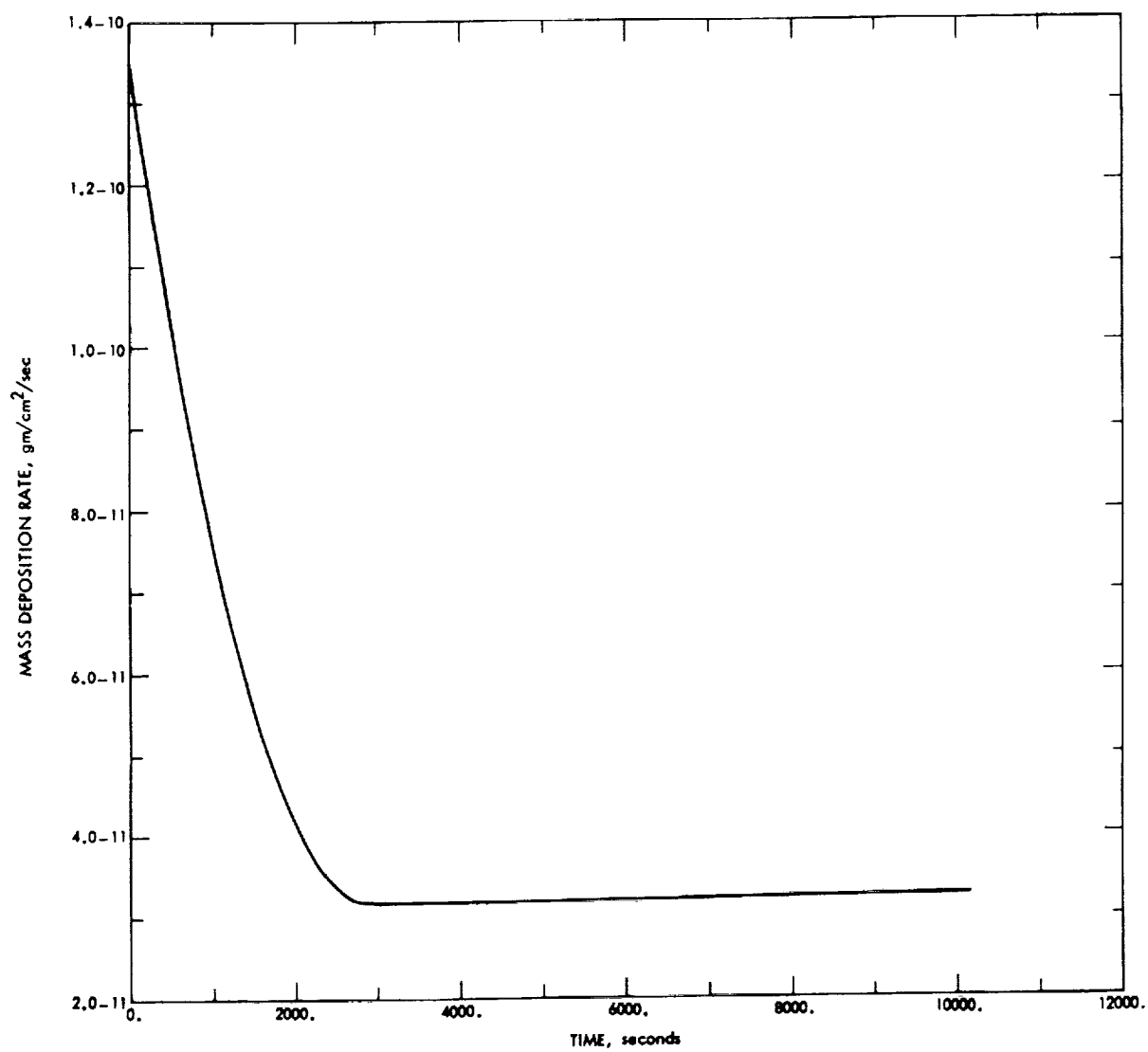


Figure B-2. Mass Deposition Rate as Derived from Figure B-1.

The Hill and Draper relation

$$\frac{d\dot{m}}{d\Omega} \bigg/ \frac{d\dot{m}}{d\Omega} \bigg|_{\theta=0} = e^{-\delta^2 (1-\cos \theta)^2}$$

can be solved for the δ which minimizes the sum of the squares of the deviations of the data from the fitted relationship. The mass deposition rate per unit solid angle from QCMs H and I is divided by that from QCM J and set equal to g_i . The "best" δ in the least squares sense can then be solved for from the relation:

$$\delta = \sqrt{\frac{\sum_{i=1}^n (\ln g_i) (1-\cos \theta_i)^2}{\sum_{i=1}^n (1-\cos \theta_i)^4}}$$

where θ_i is the angle between the nozzle centerline and the QCM i . Crystals H, I and J were used from runs 3, 5, 7, 11, 13, and 17 (a total of $n = 12$ data points) to compute $\delta = 9.59$.

DEFINITION OF SYMBOLS

A	Surface area of crystal, cm^2
C_f	Thrust coefficient, dimensionless
C_{fm}	Maximum theoretical thrust coefficient, dimensionless
C_m	QCM mass coefficient, Hz/gm
C_T	QCM temperature coefficient, $\text{Hz}/^\circ\text{K}$
f	Frequency, Hz
f_c	Natural frequency of vibration of the quartz crystal prior to mass deposition, Hz
F	Beat frequency; difference in frequency of each side of crystal doublet, Hz
\dot{F}	Time rate of change of QCM beat frequency, Hz/sec
g_i	Mass deposition rate per unit solid angle for QCM "i" divided by the mass deposition rate per unit solid angle at the plume centerline, dimensionless
m	Mass, grams
\dot{m}	Time rate of change of mass, gm/sec
\dot{m}_T	Average propellant flowrate to the thruster as determined by the piston flowmeter during a run, gm/sec
\dot{M}	Mass flux per unit area, $\text{gm/cm}^2/\text{sec}$
n	Total number of data points over which the summation is performed
N	Frequency constant, Hz-mm
t	Thickness of crystal blank, cm
T	Temperature, $^\circ\text{K}$
γ	Ratio of specific heats of the exhaust gases, dimensionless
δ	Plume spreading parameter in the analytical approximation of Hill and Draper (Ref. 31) dimensionless
θ	Angle from nozzle centerline, degrees

θ_1	Angle of QCM "I" from the nozzle centerline, degrees
ρ	Density of quartz, gm/cm ³
Ω	Solid angle, steradians

NTIS does not permit return of items for credit or refund. A replacement will be provided if an error is made in filling your order, if the item was received in damaged condition, or if the item is defective.

Reproduced by NTIS
National Technical Information Service
U.S. Department of Commerce
Springfield, VA 22161

This report was printed specifically for your order from our collection of more than 2 million technical reports.

For economy and efficiency, NTIS does not maintain stock of its vast collection of technical reports. Rather, most documents are printed for each order. Your copy is the best possible reproduction available from our master archive. If you have any questions concerning this document or any order you placed with NTIS, please call our Customer Services Department at (703)487-4660.

Always think of NTIS when you want:

- Access to the technical, scientific, and engineering results generated by the ongoing multibillion dollar R&D program of the U.S. Government.
- R&D results from Japan, West Germany, Great Britain, and some 20 other countries, most of it reported in English.

NTIS also operates two centers that can provide you with valuable information:

- The Federal Computer Products Center - offers software and datafiles produced by Federal agencies.
- The Center for the Utilization of Federal Technology - gives you access to the best of Federal technologies and laboratory resources.

For more information about NTIS, send for our *FREE NTIS Products and Services Catalog* which describes how you can access this U.S. and foreign Government technology. Call (703)487-4650 or send this sheet to NTIS, U.S. Department of Commerce, Springfield, VA 22161. Ask for catalog, PR-827.

Name _____
Address _____

Telephone _____

**- Your Source to U.S. and Foreign Government
Research and Technology.**

